

Modeling Fiber Dispersion During the Plasticizing Process in a Single Screw Extruder

by

Hector Sebastian Perez

A dissertation report submitted in partial fulfillment of
the requirements for the degree of

Doctor in Philosophy
(Mechanical Engineering)

at the

UNIVERSITY OF WISCONSIN – MADISON
2024

Date of final oral examination: 05/17/2024

The dissertation is approved by the following members of the Final Oral Committee:

Tim Osswald, Professor, Mechanical Engineering

Lih-Sheng Turng, Professor, Mechanical Engineering

Pavana Prabhakar, Associate Professor, Civil and Environmental Engineering

Lianyi Chen, Associate Professor, Mechanical Engineering

Alejandro Roldan-Alzate, Associate Professor, Mechanical Engineering

Acknowledgments

First, I would like to express my gratitude to my advisor, Prof. Tim A. Osswald, for giving me this opportunity, sharing his knowledge with me, and mentoring me in my career as an engineer. Without his guidance, I would not have been able to reach this goal successfully. I also would like to express my great appreciation to Prof. Pavana Prabhakar, Prof. Lih-Sheng (Tom) Turng, Prof. Alejandro Roldan, and Prof. Lianyi Chen for serving on my dissertation committee and for their continuous advice.

I want to thank everyone who helped me with this project, especially Paula Hohoff and Florian Hill, who assisted me extensively. I also want to express my gratitude to the undergraduate students who helped me with various aspects of this project, including Jacob Gottfried, Jack Gwertzman, Avery Burger, and Ismael Melian. In addition, I want to thank Allen Roman and Abrahan Bechara, who helped me initiate this work.

I would like to thank every current and former member of the Polymer Engineering Center for their support. I especially want to thank Sara Simon and Abrahan Bechara for being my mentors and friends throughout this journey.

This would also not be possible without the love and support of my friends in Madison, especially Lewis Handy, Jessica Pachicano, Marisa Dunning, Beth Enright, and Kelsey Hacker, Hannah Erpenbeck. Thank you for picking me up from the hospital, buying me pizza, teaching me how to dance salsa, playing soccer with me, taking me to football games, and rock climbing with me.

I would finally like to thank my family for their unconditional love and support.

List of Figures

Figure 1.1: Average material content of vehicles throughout the years [3].....	1
Figure 1.2: Normalized mechanical properties as a function of fiber aspect ratio [11]	3
Figure 1.3: Manufacturing process of a) Pultruded pellets and b) Coated Pellets.....	4
Figure 1.4: A representation of fiber breakage and dispersion during the plasticizing process.....	5
Figure 1.5: Fiber length and solid bed width versus screw length [23].....	6
Figure 2.1: Extrusion modeling methods (a) classical modeling: A – solid conveying model, B – pre-melting model, C – melting model, D – melt conveying model, E – die flow model; (b) G – continuous global mode, E – die flow model [30].....	10
Figure 2.2: (a) Flat plate model of helical screw channel. (b) Flat plate model for shallow screw channel neglecting the effect of flight walls.	12
Figure 2.3: Effect of shear rate on dispersion with respect to dimensionless time [54]	13
Figure 2.4: Effect of shear stress on dispersion by varying viscosity [54].....	13
Figure 2.5: Schematic representation of the dispersion evolution of an agglomerate depending on the infiltration level[52].	14
Figure 2.6: Fiber separation into fiber bundles and individual fibers after pyrolysis [64].	15
Figure 2.7: Image taken by Kuroda et al. showing fiber bundle mixture [65].....	16
Figure 2.8: Representation of fiber breakage occurring for (a) a low level of dispersion and (b) a high level of dispersion[63].	17
Figure 3.1: a) Mount used to scan pellets b) Measurement of fiber bundle area and perimeter using ImageJ.	18
Figure 3.2: Normalized S value with respect to a pellet's length.	20
Figure 3.3: Comparison between the average S value through the length of the pellet and the S value at the mid-plane.	20
Figure 3.4: Normalized frequency of S value for each material.	21
Figure 3.5: Procedure for embedding LFT pellets into matrix sample plaque.	23
Figure 3.6: (a) Pellets were inserted vertically in a 3D printed mount; (b) cross-section of a scan where a perimeter and area were calculated for a fiber bundle in a pultruded pellet.....	23
Figure 3.7: a) Layers of sliding plate rheometer (SPR). b) Side view of SPR with sheared sample.....	24
Figure 3.8: Mount used to scan samples with constant parameters.	25
Figure 3.9: Method by which sheared sample was scanned, and a fiber pixel weight distribution was calculated.	26
Figure 3.10: The standard deviation of the fibers' spread versus the S parameter calculated from the characterization process.	28
Figure 3.11: Schematic of Couette rheometer experimental setup.	30
Figure 3.12: Sample preparation for Couette rheometer. Sample molding (a) and Couette after sample insertion (b)	30
Figure 3.13: Mathematical representation of the dispersion process.	32
Figure 3.14: Preliminary scans of Couette rheometer experiments.....	32
Figure 3.15: Standard deviation with respect to different volume fractions.....	33
Figure 3.16: Linear relationship between standard deviation and dispersion value.	34
Figure 3.17: ROI study determining variation with respect to ROI size.	35
Figure 3.18: Sample scan of test sample with 0% and 100% dispersed samples.	35
Figure 3.19: Dispersion results comparing coated pellets with pultruded pellets.....	36

Figure 3.20: Dispersion with respect to total deformation for several experiments.	37
Figure 3.21: Linear regression showing the critical stress of fiber agglomerates.	37
Figure 3.22: Comparison between the dispersion model and experimental data.....	39
Figure 4.1: Preliminary results from screw pull-out experiments	40
Figure 4.2: Visual representation of single screw extruder used for this study.....	41
Figure 4.3: Procedure to scan extracted samples from the screw.	42
Figure 4.4: Dispersion results comparing different barrel temperature profiles.	43
Figure 4.5: Dispersion results comparing three screw velocities.....	44
Figure 4.6: Dispersion comparison of materials with different fiber content.....	45
Figure 4.7: Dispersion comparison between pultruded pellets and coated pellets.	45
Figure 4.8: Left) the material begins as a solid in the screw channel, Middle) solid to melt transition where solid width (X) is compared to channel width (W), Right) fully melted state.	47
Figure 4.9: Visual representation of material system modeled as a rectangular prism unwinding from the screw.	48
Figure 4.10: Graph of curvature factor and shallow channel factor determining where assumptions hold throughout the length of the screw.	49
Figure 4.11: Solid width ratio plotted along with dispersion values, showing dispersion begins to occur near the position where the solid width ratio is 0.6.	50
Figure 4.12: Samples from the screw pull-out experiment (30 RPM, 190-220°C) lined up continuously to show dispersion evolution.	50
Figure 4.13: Samples from the screw pull-out experiment (30 RPM, 190-220°C) lined up continuously to show the solid width ratio with respect to dispersion.	51
Figure 4.14: Visual representation of the method used to model screw channel where the barrel (Top) surface acts as a sliding wall and the screw (Bottom) surface acts as a fixed wall.....	52
Figure 4.15: Comparison between Experimental data and model for (15 RPM, 250-250°C, PPF30).....	54
Figure 4.16: Comparison between Experimental data and model for (30 RPM, 250-250°C, PPF30).....	54
Figure 4.17: Comparison between Experimental data and model for (60 RPM, 250-250°C, PPF30).....	55
Figure 4.18: Comparison between Experimental data and model for (30 RPM, 190-220°C, PPF30).....	55
Figure 4.19: Comparison between Experimental data and model for (30 RPM, 250-220°C, PPF30).....	56
Figure 4.20: Error difference between experimental values and modeled dispersion.	57
Figure 4.21: Comparison between 1D Newtonian model and 2D COMSOL model using the same fitting parameter (k).....	58
Figure 4.22: Results from the 2D COMSOL model with a different fitting parameter (k) from the 1D model.....	58
Figure 4.23: Weighted average fiber length compared to modeled fiber dispersion.....	59
Figure 4.24: Weighted average fiber length compared to measured fiber dispersion.....	60
Figure 4.25: Fiber dispersion and fiber breakage model done in Cmsol with fiber length measurements.	61
Figure 5.1: Broken pellets found at the bottom of the hopper during the screw pull-out experiment.....	64

List of Tables

Table 1: Couette rheometer experimental plan

Table 2: Screw Pull-out experimental parameters

Table 3: Average error difference percentage

List of Variables

M_z	Manas-Zloczower number
$\dot{\gamma}$	Shear-rate
ω	Vorticity
S	Shape parameter
\bar{x}	Average x-position
i	Image number
vox	Voxel size
N_f	Number of fiber pixels
ε	Dispersion percentage
k	Fitting parameter
t	Time
t_o	Time at which dispersion begins
τ	Shear stress
σ_c	Cohesive stress
n	Power fitting parameter
v_z	Velocity in the z-direction
y	y-direction
T	Temperature
η	Dynamic viscosity
L	Length
D	Diameter
Φ	Melting rate
V_{bx}	Barrel velocity in the x-direction
ρ_m	Melt density
U_2	Material parameter of power law model viscosity
k_m	Thermal conductivity of melt
T_b	Barrel temperature
T_m	Melting temperature
U_1	Material parameter of power law model viscosity
c_s	Heat capacity of solid material
T_s	Solid temperature
λ^*	Heat of fusion
X_1	Solid width at previous position
X_2	Solid width at current position
W_1	Channel width at previous position
W_2	Channel width at current position
\overline{W}_o	Average channel width

H_o	Channel height when melting initiated
G	Mass flow rate
H	Screw Channel height
z_1	Previous z-position
z_2	Current z-position
ψ	Ratio of something
A	Slope of changing channel height
H_1	Channel height when tapered section begins
H_F	Final channel height
Z_T	Helical length of tapered section
D_b	Diameter of barrel
R_b	Radius of barrel
R_s	Radius of barrel minus channel height
P	Pressure
v_x	Velocity in the x-direction
z	z-direction
V_{bz}	Barrel velocity in the z-direction
Q_p	Mass flow rate due to pressure
Q_d	Mass flow rate due to drag flow
L_W	Weight-average fiber length
$L_{W,\infty}$	Weighted equilibrium fiber length
$k_{f,W}$	Fitting parameter for the fiber breakage model

Table of Contents

Acknowledgments	i
List of Figures	ii
List of Tables	iv
List of Variables.....	v
Abstract.....	ix
1. Introduction	1
1.1 Long Fiber-Reinforced Thermoplastics	3
1.2 Motivation and Objectives.....	5
1.3 Structure and Scope	7
2. State of the Art.....	9
2.1 Studies on Modeling a Single Screw Extruder	9
2.2 Studies on Agglomerate Dispersion.....	12
2.3 Studies on Fiber Dispersion and Breakage.....	15
3. Fiber Dispersion	18
3.1 Single Pellet Dispersion	18
3.1.1 Pellet Morphology Characterization.....	18
3.1.2 Sliding Plate Rheometer.....	22
3.1.2 Dispersion Characterization.....	24
3.1.3 Results.....	27
3.2 Multi-Pellet Dispersion	29
3.2.1 Couette Rheometer	29
3.2.2 Dispersion Characterization.....	31
3.2.3 Results.....	35
3.3 Modeling Fiber Dispersion for Couette Rheometer.....	37
4. Modeling Fiber Dispersion in Single-Screw Extruder	40
4.1 Screw Pull-out Experiments	40
4.2 Modeling Single Screw Extruder	46
4.3 Modeling Fiber Dispersion.....	50
4.4 Validation of Fiber Dispersion Model.....	54

4.5 Fiber Length Measurements.....	59
5. Summary	62
5.1 Recommendation for Future Work	63
5.2 Publications.....	64
6. References	65

Abstract

Understanding the mechanics of fiber attrition during the extrusion process is highly important in predicting the strength of long fiber-reinforced thermoplastics composites. However, little work has been done to investigate the mechanics of fiber dispersion and its effects on fiber attrition. This study investigates fiber dispersion during the extrusion process of LFT pellets. In order to validate our modeling approach, two new fiber dispersion measurement techniques were developed using micro-CT tomography. LFT samples were then subjected to simple shear flow using a sliding plate rheometer and Couette rheometer. Based on the findings, a time-dependent dispersion model is proposed and validated using experimental data. A dispersion model is then proposed for single screw extruders to predict fiber dispersion. Screw pull-out experiments were performed to determine fiber dispersion along a single screw extruder. The model predicts fiber dispersion due to hydrodynamic stresses along the helical length of the screw geometry. Results showed good agreement with experimental measurements. Fiber length measurements were also performed on samples taken from the screw pull-out experiments. Results indicate that both dispersion and breakage occur simultaneously after a critical point of melting has occurred.

1. Introduction

Lightweight materials are becoming increasingly important in industries such as the automotive, construction, and aerospace industries due to their weight-to-strength ratio, processability, recyclability, and cost [1–3]. As a result, any advancement to a material in these criteria is a leap in technological progress for an industry. As automobiles remain one of the leading transportation methods worldwide, the importance of lowering a vehicle’s weight has never been more significant due to carbon emissions. It is generally believed that for every 10% a car reduces its weight, the fuel consumption reduces by 5-7% [4]. Automakers are incorporating more polymers and polymer composites in automobiles to reduce vehicle weight [2–7]. As shown in Figure 1.1, the overall percentage of polymer/composite material in a vehicle has steadily been increasing from 7% in 1977 to 12% in 2015 for automobiles [3]. This, in part, is due to an advancement in technology and understanding of composite processing that has allowed composites to increase their strength and replace other materials in a vehicle.

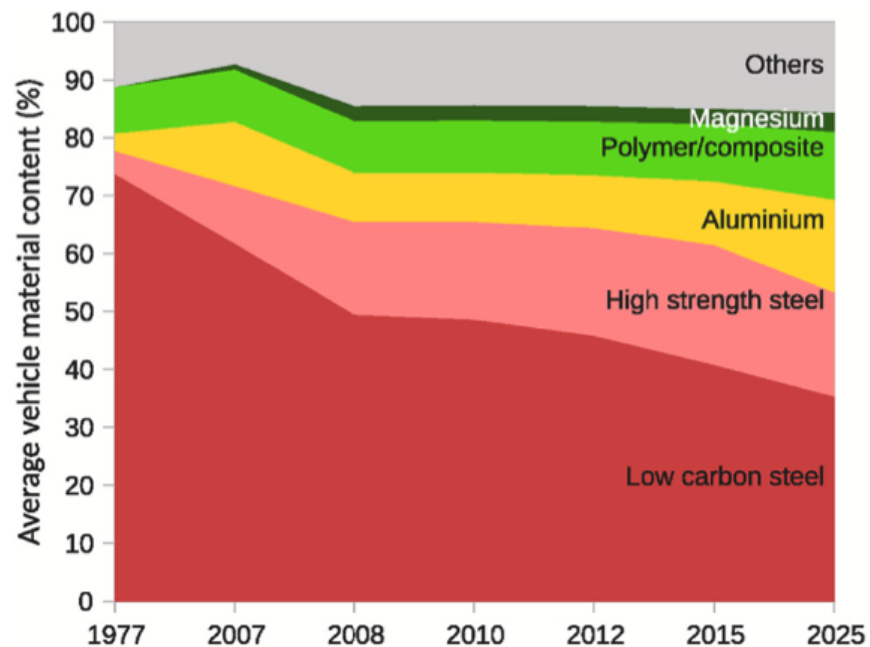


Figure 2.1: Average material content of vehicles throughout the years [3]

In light of the recent advancements and the rapid growth of the electric vehicle (EV) industry, the study of fiber attrition within composite materials has also become increasingly vital. As EVs become more popular due to their marketability as an environmentally sustainable option, there is a heightened focus on enhancing vehicle efficiency and range. This enhancement is often achieved by lowering the weight of the vehicles and optimizing a material's build quality. This is where fiber-reinforced thermoplastic composites have become an advantageous alternative for the EV industry for two primary reasons [5,6]. One, as previously explained, composites have become a major alternative to decrease vehicle weight while still maintaining robust mechanical properties [5]. Two, with the addition of fire-retardant particles, fiber-reinforced thermoplastic composites have the thermal stability and strength needed to replace many safety components that previously couldn't be replaced with fiber-reinforced composites[6].

There are three main types of fiber-reinforced thermoplastic composites: short fiber-reinforced thermoplastics (SFTs), long fiber-reinforced thermoplastics (LFTs), and continuous fiber composites (CFCs). SFT materials are often very easy to process as the short fiber length allows the material to be injection molded easily, but they lack mechanical properties due to the short length of fibers and their anisotropic effects [8–11]. CFC materials, on the other hand, lead to a significant improvement in mechanical properties but are often difficult to process in complex geometries. LFT materials represent a compromise between processability and mechanical properties as they can be injection molded, compression molded, and extruded while maintaining relatively high mechanical properties [9,12,13]. However, both LFTs and SFTs are prone to have their microstructure properties affected due to their processing method. Predicting the microstructure of composites from their process parameters would allow for the optimization of said parameters and improve the end-product properties.

1.1 Long Fiber-Reinforced Thermoplastics

As previously stated, LFTs represent the bridge between the processability of SFTs and the mechanical properties of CFCs. Schemme summarized the effect of fiber aspect ratio on a composite's normalized mechanical properties in Figure 1.2 [11]. While LFTs have been around for over three decades, advancements are still being made to optimize the manufacturing process, improve mechanical properties, and lower production costs [1,9].

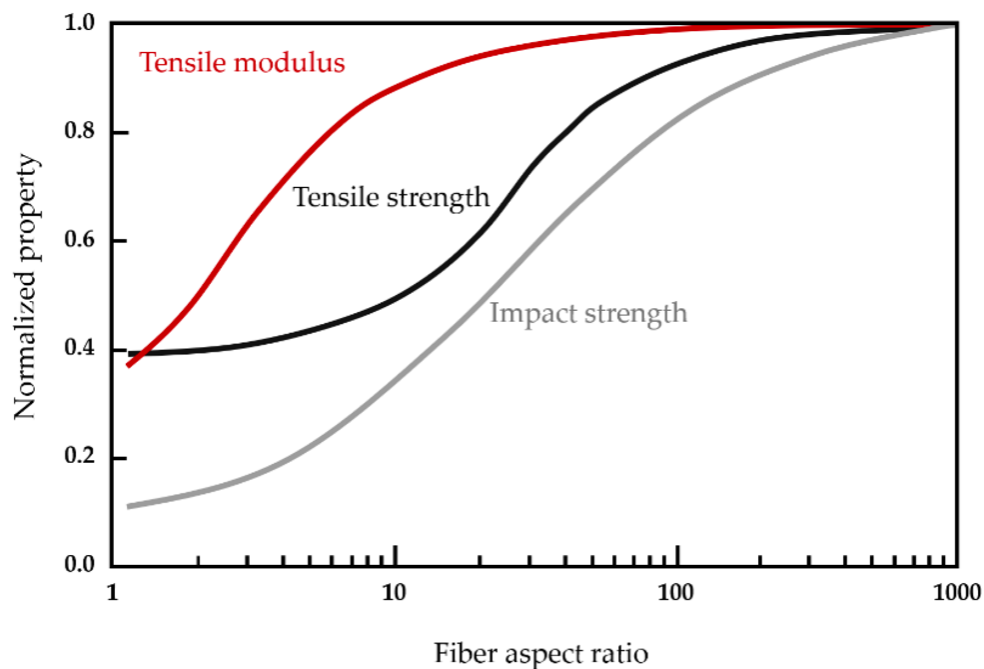


Figure 1.2: Normalized mechanical properties as a function of fiber aspect ratio [11]

It is well known that processing LFTs in the extrusion, injection, and compression molding processes severely damages fibers [9,11,14–20]. Therefore, many studies done using LFTs focus on the effect process parameters have on fiber attrition. Optimizing manufacturing processes can help improve a composite's mechanical properties by reducing fiber attrition during the processing.

LFTs are commonly supplied in pellet form and can be manufactured with wire coating, crosshead extrusion, and pultrusion techniques. Pultruded LFT pellets are manufactured by pulling several rovings of fibers through an impregnation die where the rovings are impregnated with the polymer [12,21]. This technique often spreads the rovings with the dies, creating a greater fiber-matrix interface area which may lead to a more uniform fiber distribution [22]. Coated LFT pellets are manufactured by pulling a single roving of fibers through an impregnation die. Parts produced with these types of pellets have been found to have a longer fiber length average compared to parts produced with pultruded pellets [10,12,17]. However, studies have also found that coated pellets lead to fiber bundles in the production of parts with said material, which leads to weaker parts [22]. Figure 1.3 shows how the manufacturing process affects the morphology of the fiber bundle within the pellets, showing that pultruded pellets have a better spread of fibers than coated pellets.

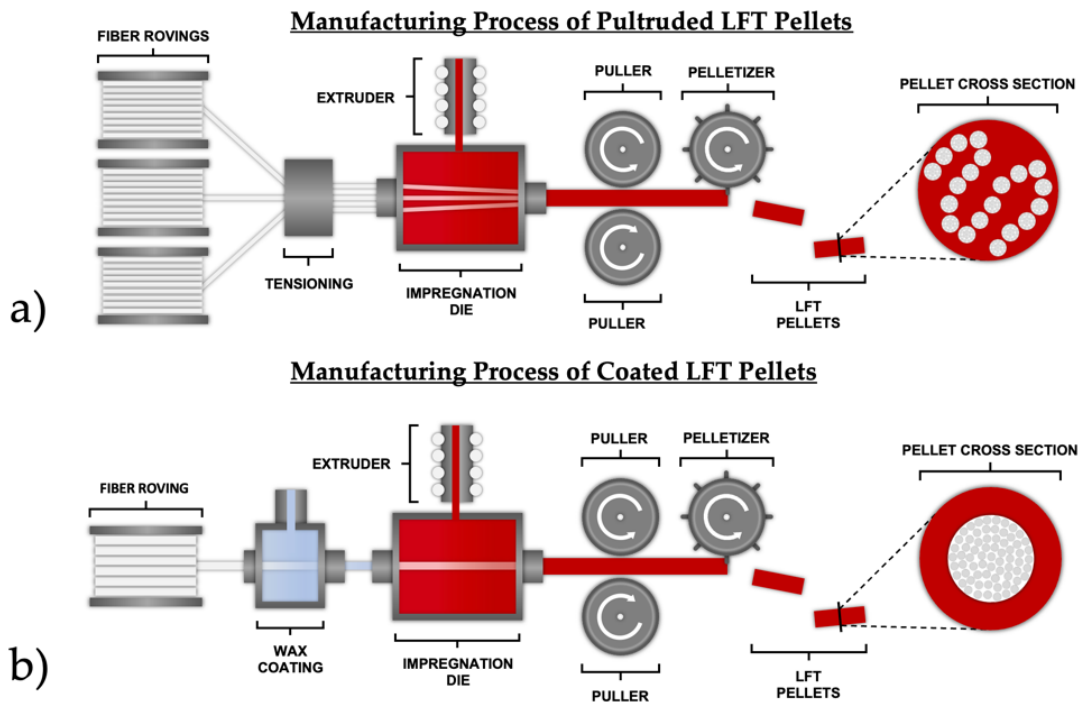


Figure 1.3: Manufacturing process of a) Pultruded pellets and b) Coated Pellets.

1.2 Motivation and Objectives

The material properties of fiber-reinforced composites depend on the overall fiber length, concentration, orientation, and surface adhesion properties of the final product [8,11]. While past research efforts have mostly focused on analyzing fiber orientation, concentration, and length, little work has been done to study fiber dispersion and its effects during processing.

There are two main reasons for studying fiber dispersion during the processing of LFTs. First, these materials are being used to extrude different structural profiles for the construction industry, given their good impact and creep resistance in combination with their cost-effectiveness. The level of stress expected from the extrusion process is low enough that excessive fiber damage is not the main concern [15]. However, this low level of stress leads to poor dispersion, which causes problems when regions of extruded or injection-molded components have fiber bundles [10,15,22]. Second, previous work has shown that undispersed fiber bundles can be a source of stress concentration in injection molded parts [16,22,23]. The reason is that a fiber bundle produces dry surface areas that have no adhesion to the polymer, which weakens the part. Hence, optimizing dispersion while reducing fiber damage is vital for increasing the mechanical performance of components molded with LFTs. Figure 1.4 illustrates the coupling effect of fiber breakage and dispersion during the plasticizing process.

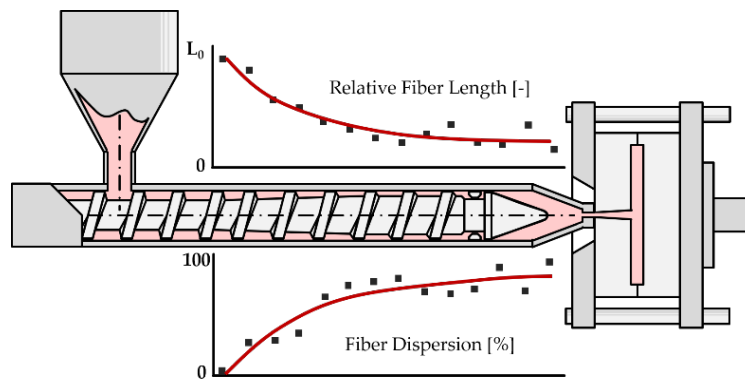


Figure 1.4: A representation of fiber breakage and dispersion during the plasticizing process

Understanding the dynamics of fiber dispersion and its relationship with fiber breakage also plays a crucial role in material selection. Pultruded pellets are often the preferred type of material due to an increase in “wet fibers,” referring to a fiber having surface interfaced with the polymer material [12,21,23]. Pellets manufactured using a wire coating technique are believed to maintain a longer fiber length due to the polymer coating acting as a protecting layer and requiring simple machines to manufacture[12,17]. However, it has also been found that the use of coated pellets can lead to parts containing undispersed fiber bundles [14–16,20,23]. There are studies that have evaluated the mechanical properties of parts with a low level of fiber dispersion that have shown a decrease in strength [16,22,24]. This low level of mechanical properties has been attributed to the poor adhesion between fibers and polymer. On the contrary, a study done by Von Turkovich[19] showed no effect of fiber dispersion on mechanical properties.

While the effect of fiber dispersion on a part’s strength is not entirely clear, many studies have attributed a long fiber length to poor dispersion [10,12,15,23]. A study done by Wolf [23] showed that much of the fiber attrition occurs in the interface between the solid bed and the molten material, which the author attributes to the poor dispersion and high shear stresses happening simultaneously, as shown in Figure 1.5.

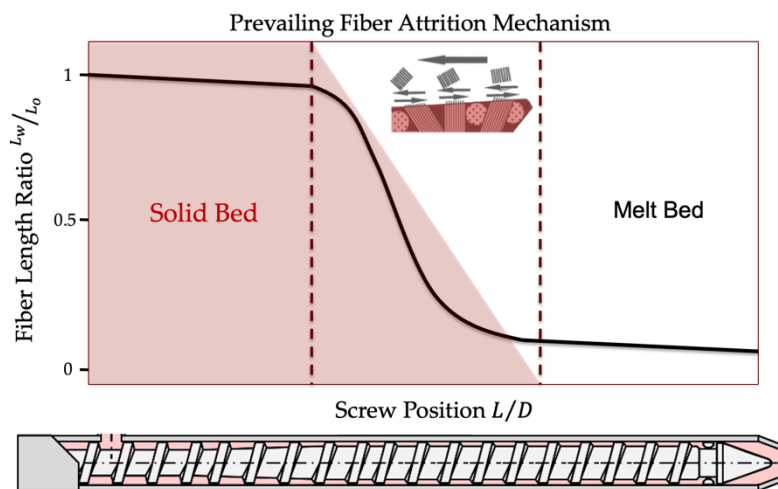


Figure 1.5: Fiber length and solid bed width versus screw length [23]

According to their study, Ren and Dai [25] noticed that fiber length decreases as fiber dispersion increases. This means there is evidence showing that fiber dispersion plays a significant role in determining the evolution of fiber length during the plasticizing process. The fact that there is no current model to predict fiber dispersion makes the study and development of a fiber dispersion model imperative to fully understand fiber attrition during the processing of LFTs.

1.3 Structure and Scope

In order to fully understand fiber attrition, it is essential to predict fiber dispersion as well. A dispersion model would not only be beneficial for understanding fiber length, but development could also decrease processing time and lead to better screw and material design. To achieve this objective, the following steps were taken:

- i. The morphology of a pellet was be studied and characterized to determine the effects of material production techniques on dispersion. Pellets will be tested using a sliding plate rheometer to apply an equal deformation to each pellet. Pellets will be scanned using a μ -CT Scanner to characterize pellet morphology and the final dispersion value.
- ii. A multi-pellet dispersion study was be done using a Couette rheometer to isolate the effects of process conditions such as residence time, shear rate, and viscosity. A noble method to characterize dispersion for a multi-pellet system will be developed to measure dispersion levels. The resulting data will be used to propose an initial dispersion model.
- iii. A single screw extruder was used to measure fiber dispersion within the screw. Dispersion will be measured by implementing screw pull-out experiments and taking samples throughout the screw to measure

dispersion. Experiments will be designed to test temperature profiles, screw velocity, and morphological parameters.

- iv. Finally, a mathematical model to describe fiber dispersion was proposed. This model will be coupled with existing melting models to determine the position at which dispersion begins to occur in the process.

2. State of the Art

2.1 Studies on Modeling a Single Screw Extruder

In the polymer processing industry, the most commonly used technology is a single-screw extruder, which is also found in an injection molding unit and can be used for a variety of applications, such as blow molding, wire coating, and film blowing [25–30]. While this technology has existed since the 19th century, it has still been challenging to model the entire process to this day [29–33]. The extrusion process can be divided into three phases: solid conveying, polymer melting, and the melt conveying stage. The melt conveying phase has been well studied and understood using the equations of continuity and motion. However, the solid conveying and polymer melting phases are still not well understood and remain a large focus for extrusion research [29,30].

To model the evolution of material as it plasticizes through an extruder, each phase of the extruder must be modeled separately to determine shear stresses, pressure, energy consumption, etc., as shown in Figure 2.1.a [30]. While global modeling techniques, Figure 2.1.b, have been successful in the past [30,34], they are still considered to be in their early stages, as the Discrete Element Method (DEM) has been found to be preferred for the solid conveying phase while Computational Fluid Dynamics (CFD) were found to perform better during the melting phase of extrusion [30].

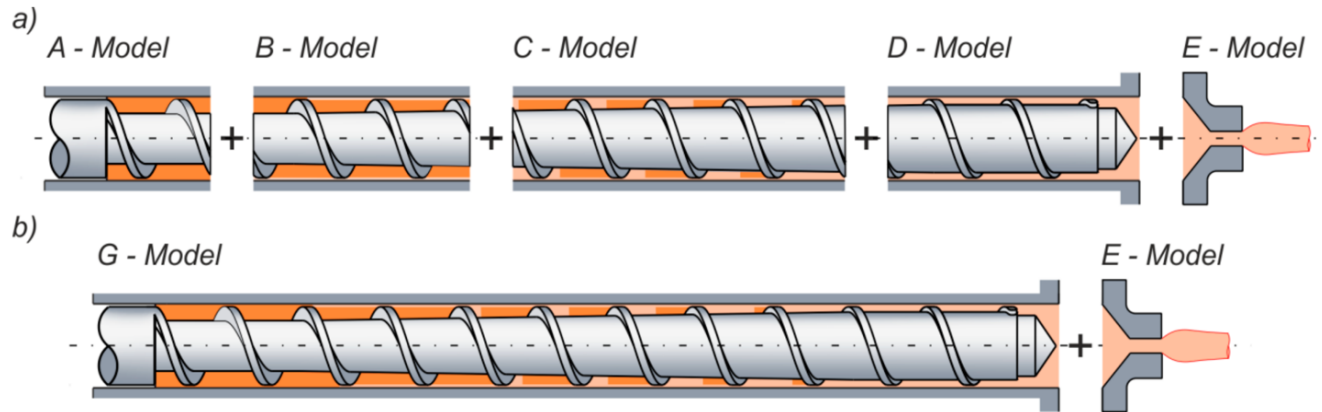


Figure 2.1: Extrusion modeling methods (a) classical modeling: A – solid conveying model, B – pre-melting model, C – melting model, D – melt conveying model, E – die flow model; (b) G – continuous global mode, E – die flow model [30].

The first model depicting the solid conveying phase was proposed by Darnell and Mol in 1956, where it was assumed that the solid particles are rapidly compacted and form a non-deformable solid bed [30,35]. With time, other researchers have extended the model proposed by Darnell and Mol. In 1968, Schneider introduced anisotropic coefficients to implement a non-distributed pressure in the bulk material [36]. The angle of the force pressing on the solid bed was also found not to be normal to the direction of the flight in the screw by Hyun et al. [37]. An energy balance was then considered by Tadmor et al., to define the heat conduction applied to the solid particles [31–33,38–40]. While many researches have extended the work of Darnell and Mol, the primary analysis of the solid-conveying phenomena has remained the same [30].

The first study of the melting process was done in 1959, in which Maddock and Street implemented the screw pull-out technique to analyze the melting evolution within an extruder [41,42]. This was done by stopping the screw, rapidly cooling the screw, dumping water on the barrel, pulling the screw out of the barrel, and analyzing the cross-section of the polymer in the screw channel [30,41]. As screw pull-out experiments are difficult, time-consuming, and expensive, new methods have been developed to experimentally analyze the melting mechanism. In 2001, Zhu used glass windows in the

barrel to study the melting phenomena [43]. Noriega et al. added cameras looking inward into the barrel to determine the melting profile [44]. After Maddock and Street's study, Tadmor et al. proposed the first melting model in 1970 [38]. This melting model was based on defining the velocity and temperature profile of the melt film and solid bed to implement an energy balance between the melt and solid interface [31,32]. Using this model, the first computer extrusion program was developed and became an essential contribution to the field of extrusion modeling [30,45]. Three-dimensional models have also been attempted without relying on any previous melting models [34,46,47]. In the case of Viriyayuthakorn et al. and Syrjala, models were not verified with experiments [46,47]. In 2018, Wilczyński et al. developed a global modeling technique that implements all phases of the plasticizing process and was verified with experimental studies [30,34]. This model does not align with Tadmor's melting model, which Wilczyński attributes the difference to the slipping of particles in the screw/barrel surfaces [30–32,34].

While the melt-conveying phase can be well modeled using the equations of motion, research on this phase mostly focuses on simplifying modeling techniques [26,30,48]. For example, an extruder is often modeled by assuming a stationary screw with a moving barrel [31,38,48,49]. This was proved to work by Rauwendaal et al. when the screw channel is small relative to the barrel diameter [48,49]. In addition to neglecting curvature in a shallow channel, the effect of flight walls can also be neglected when the width of the screw channel is large relative to the height of the channel [31,38,48,50]. When the screw channel is small relative to both the screw channel and the barrel diameter, the screw can be modeled as two infinite parallel plates where one plate is stationary, and the other plate moves at the same speed as the barrel, as shown in Figure 2.2 [25–28,31,48,51]. These assumptions have made modeling melt conveying simpler and have been found to be acceptable approximations by various studies [25–28,31,48,51].

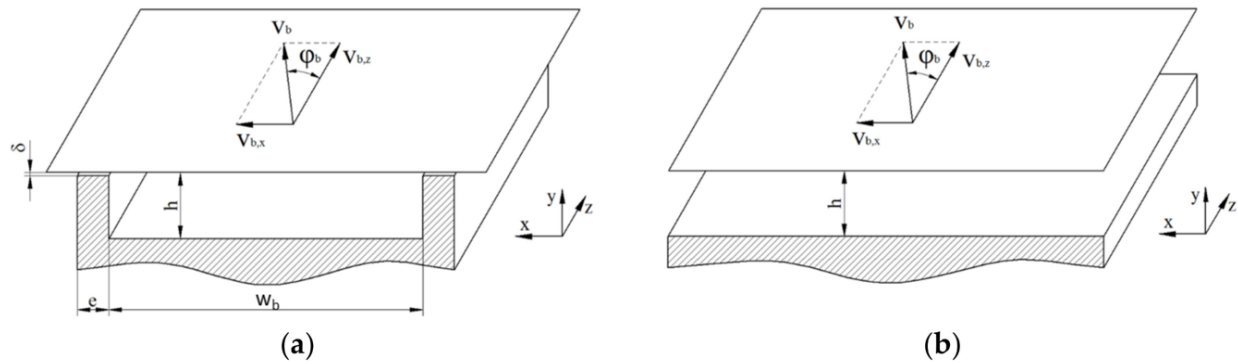


Figure 2.2: (a) Flat plate model of helical screw channel. (b) Flat plate model for shallow screw channel neglecting the effect of flight walls.

2.2 Studies on Agglomerate Dispersion

Many fillers used in the composites industry initially start in the form of aggregates. These aggregates can vary in the form of many materials, such as wood, rubber, carbon, or glass [52]. However, manufacturers generally provide aggregates in the form of clusters called agglomerates. This is done as it takes the process of incorporating the fillers into the polymer away from the customer, and often, these agglomerates already have a level of dispersion when they are provided in the form of pellets [52]. Agglomerates, however, pose a problem when they are not processed correctly, which can lead to the potential mechanical properties of a composite not being achieved.

Studies have isolated the mechanisms that cause agglomerate dispersion. Many studies, like the one by Manas-Zloczower [26] (Figure 2.3), have shown that shear rate has no effect on the dispersion value if total deformation is equal and all other parameters remain constant [52–56]. While many studies agree that dimensionless time, also known as total deformation, is the main driver for dispersion, there is little agreement as to the overall magnitude of shear stress on dispersion. Powell [53] found no difference in dispersion values when varying the shear stress. Manas-Zloczower [52,54,57] found that

not only does shear stress influence dispersion (Figure 2.4), but it also dictates the kind of dispersion that occurs.

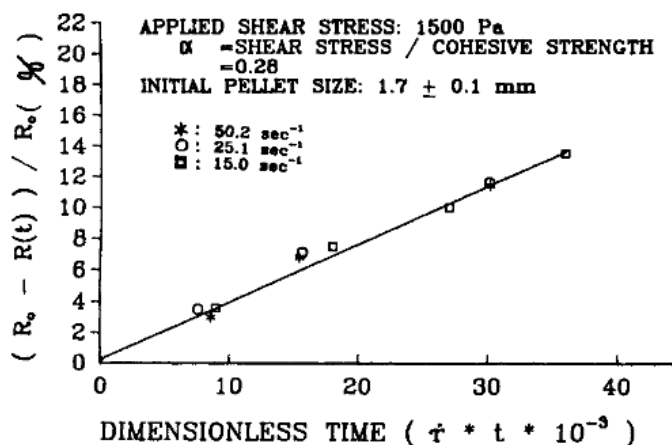


Figure 2.3: Effect of shear rate on dispersion with respect to dimensionless time [54]

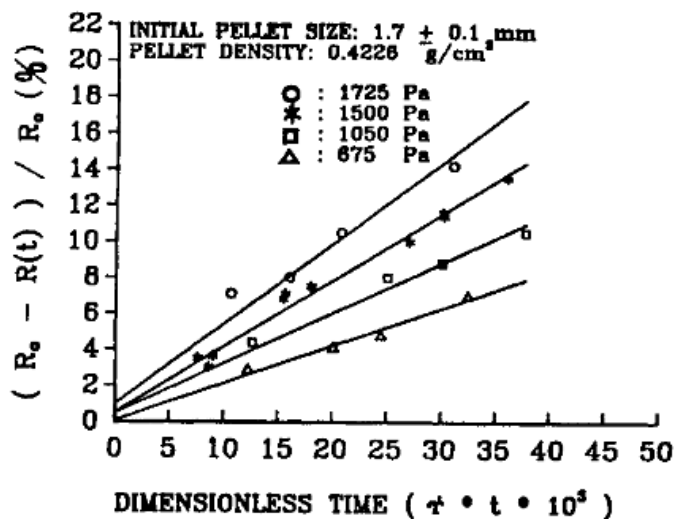


Figure 2.4: Effect of shear stress on dispersion by varying viscosity [54]

As shown by Manas-Zloczower, dispersion can occur in two forms: erosion and rupture [52,54,57,58]. Erosion is a slow form of dispersion where individual aggregates separate from the agglomerate. Rupture is a quick form of dispersion where agglomerates break off into smaller agglomerates. Both forms of dispersion were found to be caused by the ratio between hydrodynamic shear stress and critical stress, which acts as the minimum amount of stress taken to begin the dispersion process [52,54,56,58,59]. Because

this phenomenon happens in a stochastic manner, it is often modeled with a combination of statistical models and flow fields [60]

The infiltration process of an agglomerate has also been found to affect the magnitude of the force required to disperse agglomerates [52,61]. In a study done by Lee et al. it was found that for some types of agglomerates, a higher level of matrix infiltration decreased the amount of force required to disperse the agglomerates [52]. This occurs as hydrodynamic shear stress peels away the wetted region of an agglomerate, bringing the dry material with it. Figure 2.5 shows a representation of the evolution of an agglomerate depending on its infiltration level [52].

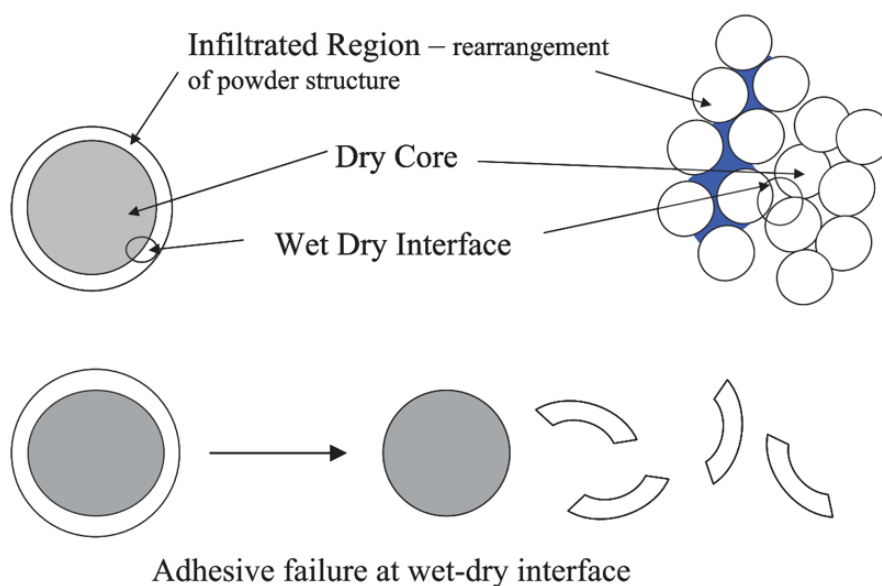


Figure 2.5: Schematic representation of the dispersion evolution of an agglomerate depending on the infiltration level[52].

All the methods of dispersive mixing that have been mentioned up to this point are with respect to simple shear flow, however, it has been found through several studies that elongational flow is more effective at dispersing mixtures than simple shear flow. The Manas-Zloczower number has been proven to be useful, as it helps distinguish the kind of dispersive mixing that is happening and can be used to predict if a flow will be effective at dispersing[52,53,58,62]. The Manas-Zloczower number is shown by equation

1, where the flow can be characterized as elongational when it equals 1.0, simple shear when it equals 0.5, and no deformation when it equals zero[52,59].

$$M_z = \frac{\dot{\gamma}}{\dot{\gamma} + \omega} \quad (1)$$

2.3 Studies on Fiber Dispersion and Breakage

Very little work has been done to understand the fiber dispersion process as it is difficult to relate to agglomerate dispersion theories due to the geometry of the E-glass fibers. Despite the low amount of research on dispersion, several studies have found that it has a large effect on overall fiber length[14–16,23,24,63]. As fiber length is a more popular topic of research, most studies tie in the connection between fiber dispersion and length.

The most recent attempt to measure and characterize dispersion was done by Ren et al., where screw pull-out samples were put through pyrolysis, and the remaining fibers were separated between fiber bundles and individual fibers, as shown in Figure 2.6[64].

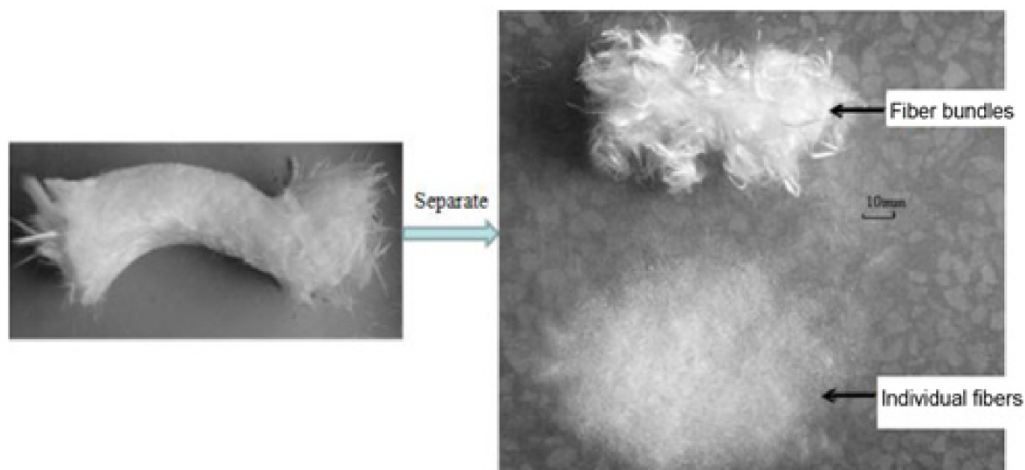


Figure 2.6: Fiber separation into fiber bundles and individual fibers after pyrolysis [64].

Ren et al. then calculated the mass of the individual fibers in comparison to the total mass and used that as the percentage of dispersion[64]. While this is a very analytical approach to measure dispersion it is quite unclear how individual fibers are separated from fiber

bundles without adding more dispersion to the system. To add to the problem, fiber bundles shown in Figure 2.6 also show some level of dispersion that is not considered for their measurement[64].

Kuroda et al. proposed another method to measure dispersion. In this method, optical images of samples were taken, and the fraction of fibers still in bundles was counted and divided by the total number of fibers in the image[65]. Figure 2.7 shows an image from the study, showing that some fibers are still in their original bundles [65].

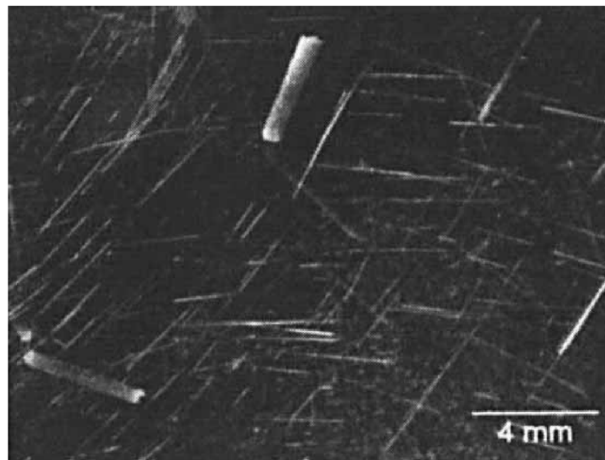


Figure 2.7: Image taken by Kuroda et al. showing fiber bundle mixture [65].

While the images clearly show the difference between fiber bundles and individual fibers, it was noted in the study that some bundles had a level of separation that could be considered two individual bundles, blurring the line between a subjective and analytical approach for measurement[65]. Advancements in fiber dispersion were also made in the same study as researchers tested fiber bundles based on their morphological characteristics, finding that bundles with an area larger than 2 mm^2 tended to disperse much slower[65]. The same study also found that fiber bundles require at least 10 kPa of shear stress to initiate the dispersion process[65].

Studies done by Bechara et al. [14,63] and Wolf [23] showed that fiber attrition is more significant when undispersed fiber bundles are subjected to high shear stresses. Bechara et al. attributed the more rapid fiber breakage to the low dispersion level of fiber

bundles [63]. Figure 2.8 shows a representation of how undispersed fibers break at a larger pace as entire fiber bundles are cut as opposed to single fibers [63]. These same findings were concluded by Wolf. However, the author attributed this sharp decline in fiber breakage to the melt/solid interface, where the fast-moving melt pool broke off fibers from the undispersed bundles, which acted as anchors [23]. These can also be seen in Figure 1.4, where Wolf found a sharp decline in fiber length in the same axial position as the material was transitioning from a solid to a melted state [23].

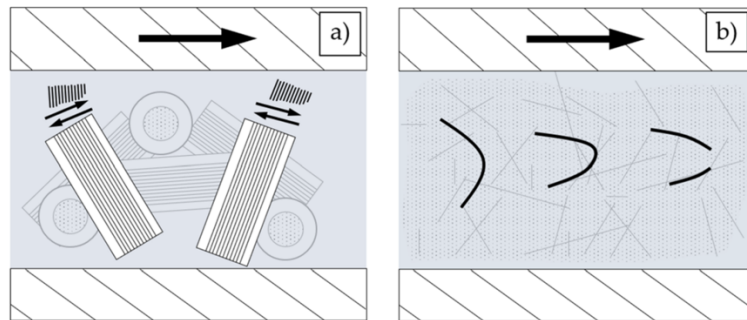


Figure 2.8: Representation of fiber breakage occurring for (a) low level of dispersion and (b) a high level of dispersion[63].

3. Fiber Dispersion

3.1 Single Pellet Dispersion

3.1.1 Pellet Morphology Characterization

This study aims to analyze the internal structure of fiber bundles within an LFT pellet. To characterize the material, pellets with varying fiber concentrations (PPGF20, PPGF30, and PPGF40) were scanned using X-ray microcomputed tomography (μ CT) to determine the boundaries of the fiber bundles and the matrix. The voxel size was maintained constant throughout the scans at $37.85 \mu\text{m}/\text{pixel}$. This voxel size was used in all the characterization scans to ensure pixel resolution was not a variable. A mount was manufactured to scan pellets vertically to ensure the pellet's cross-section was scanned properly (Figure 3.1.a). Once pellets were scanned, the fiber bundles were characterized by measuring the bundle's outer perimeter and the fiber bundle's area using ImageJ (Figure 3.1.b). The perimeter of the fiber bundle signifies the boundary layer between the fibers and the matrix. The area of the fiber bundle signifies the amount of fiber content spread by either sizing or air.

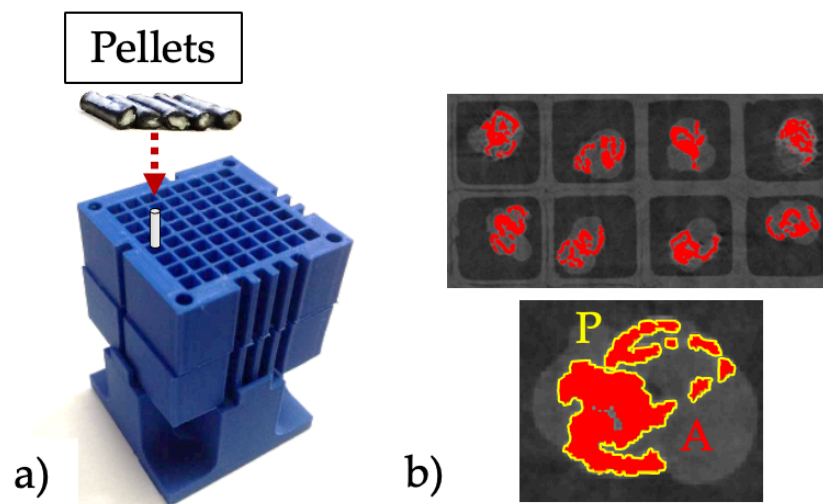


Figure 3.1: a) Mount used to scan pellets b) Measurement of fiber bundle area(A) and perimeter(P) using ImageJ

To measure both the perimeter and the area, a color threshold is implemented to distinguish between the matrix and the fibers. To ensure that the threshold designated is adequate, 25 pellets were measured for area to calculate an average area. Once the area for all pellets was within a 10% margin of the average area, then the threshold was approved. This was done as the fiber content is the same for each kind of pellet; significant differences in areas would signify different fiber contents for each pellet, which is not the case. The perimeter was only measured in the outer layer of the bundle as inner voids could not be distinguished between air, matrix, and sizing used by the provider. Because the pellets were of different sizes, a dimensionless parameter S was used to compare the smaller pultruded pellets to the larger coated pellets, where S is the perimeter of the fiber bundle squared divided by the area of the fiber bundle as shown by equation 2.

$$S = \frac{Perimeter^2}{Area} \quad (2)$$

The S parameter is a modified circular shape factor often used to describe the shape of objects compared to a circular shape. The parameter can also calculate a value for each type of shape regardless of size. A circle will always have an S parameter of 12.56 regardless of size; a square and an equilateral triangle of the same area will have an S parameter of 16 and 20.78, respectively. The dimensionless parameter is then calculated at 350 cross-sections for the coated pellets and 300 cross-sections for the pultruded pellets.

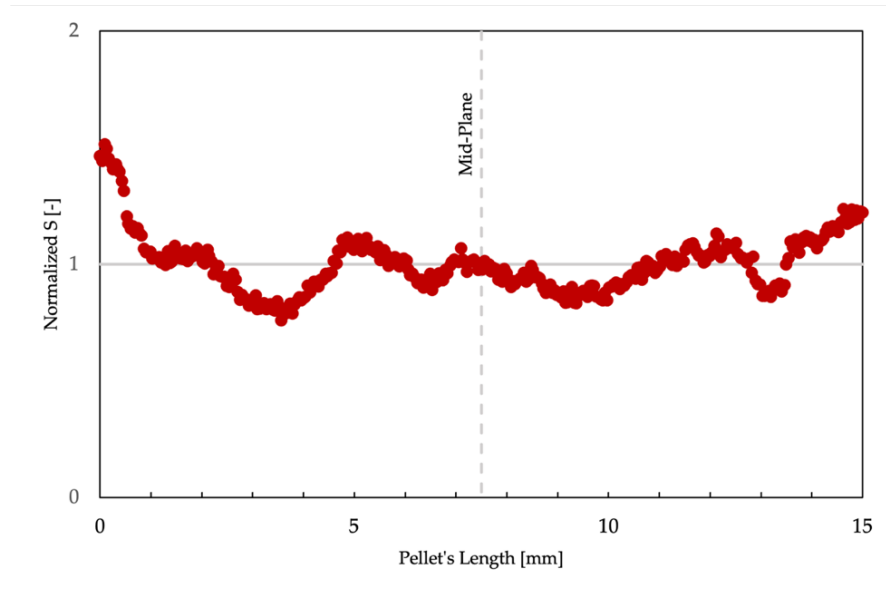


Figure 3.2: Normalized S value with respect to a pellet's length

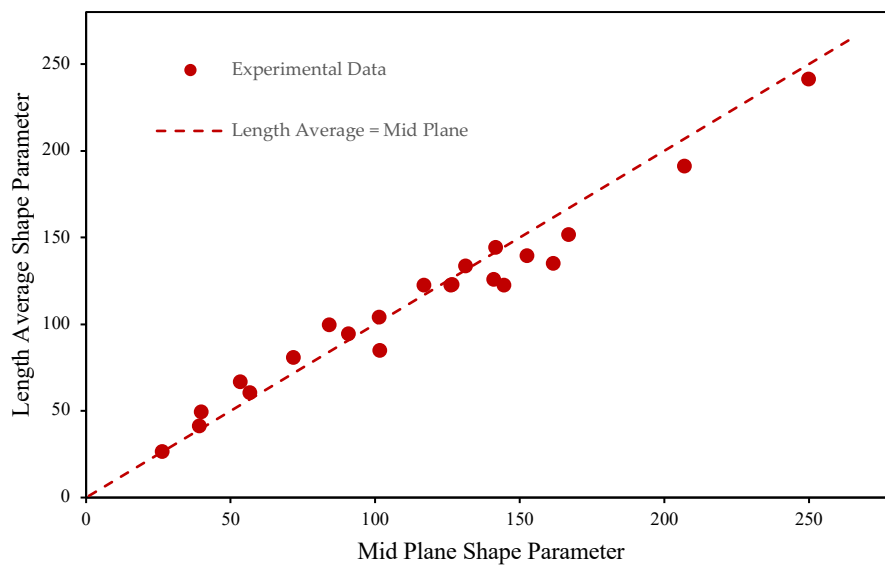


Figure 3.3: Comparison between the average S value through the length of the pellet and the S value at the mid-plane

A graph of the shape parameter normalized throughout the length of a coated pellet can be seen in Figure 3.2. After analyzing several pultruded and coated pellets, it was found that the dimensionless parameter at the midplane of a pellet is a good indicator of the average shape parameter of a pellet. Figure 3.3 shows a graph of the average S parameter

compared to the midplane S parameter, where the dashed line represents the point where the midplane and length average S parameters are equal. The midplane shape parameter was then used as the characterization parameter, allowing for more rapid characterization of LFT pellets. A population shape parameter distribution was obtained for each type of pellet used for studies in this proposal. One hundred ninety-two pellets were characterized for each type of pellet to develop a distribution curve of the S parameter for each type of pellet, shown in Figure 3.4. It is important to note that all the coated pellets have the same fiber content but differ in the amount of polymer material used to coat them. This indicates that the more significant amount of polymer leads to fiber bundles separating or deforming during manufacturing. These results also indicate that pultruded pellets have fibers with a more extensive wet surface interface than coated pellets with the same fiber content.

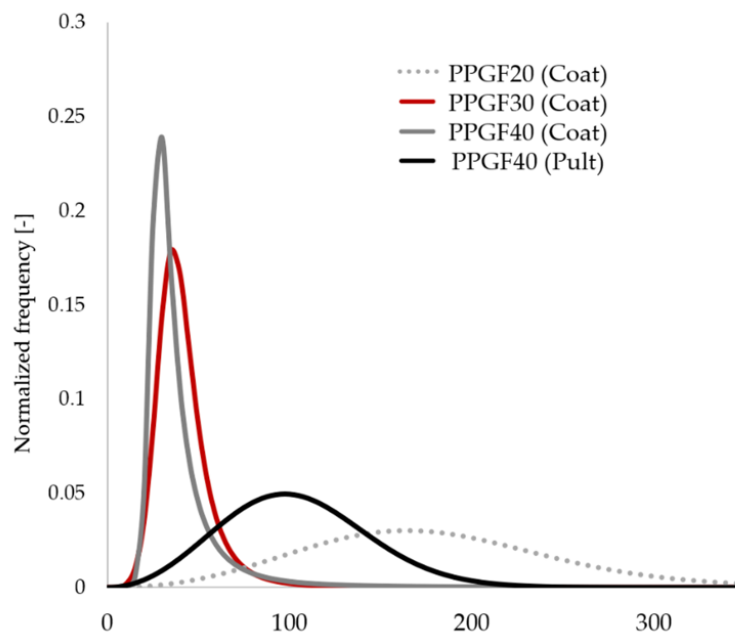


Figure 3.4: Normalized frequency of S value for each material

3.1.2 Sliding Plate Rheometer

This study investigated the initial dispersion phenomena of individual pellets to better understand the morphological effects on dispersion. To remove as many complexities as possible, a sliding plate rheometer (SPR) was used to apply a shear deformation to the pellets. Experiments were done using a constant temperature, deformation rate, and total deformation. This study allowed isolating the effects of a bundle's shape and size on its dispersion rate. Once a deformation has been applied, dispersion will be measured (Figure 3.5).

Initial sample plaques were made from virgin matrix material, where characterized pellets would later be implanted. The initial plaques of 50 mm × 125 mm × 2.16 mm were compression molded using a hot press heated up to 220°C and at a clamping force of 4.45 kN. Initial plaques were first made with the absence of pellets to avoid porosity from forming and to accurately place the pellets in the correct orientation during the compression molding process. Once the plaques were manufactured, a die punch was used to make two cavities perpendicular to the direction of the flow at the center of the plaque, as shown in Figure 3.5. Cavities were made perpendicular to the flow direction to test the characterized cross-section with respect to the principal straining axis. Pellets were placed in the cavities and merged with the matrix material using the hot press. This allows the pellet to be surrounded by matrix material while conserving the original shape and orientation of the pellet. To ensure the compression molding process did not alter the characterization parameters of our samples, a scan was done on a sample plaque after implanting the pellet using the compression molding machine. The scans showed no significant alteration in the shape of the fiber bundle within the sample plaque as a result of the experimentation process. Figure 18 shows a fiber bundle during the characterization process (Figure 3.6.a), and once implanted into the matrix plaque (Figure 3.6.b). It can be appreciated that the shape of the fiber bundle does not significantly change during the sample preparation process.

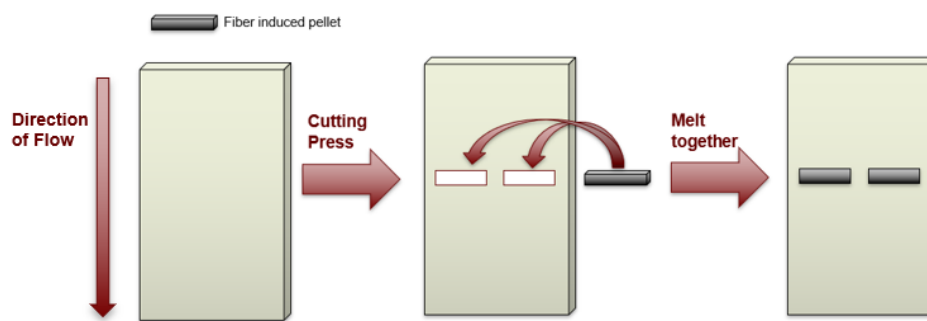


Figure 3.5: Procedure for embedding LFT pellets into matrix sample plaque.

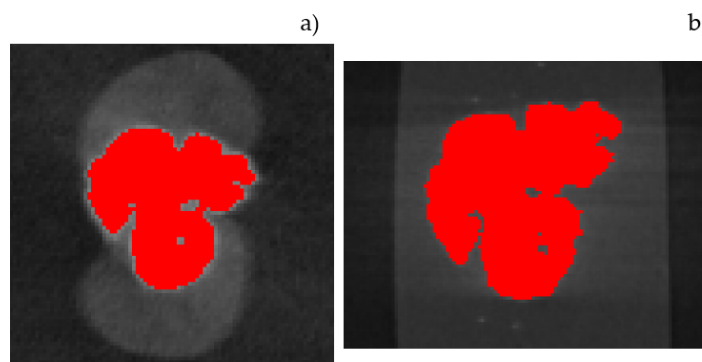


Figure 3.6: (a) Pellets were inserted vertically in a 3D printed mount; (b) cross-section of a scan where a perimeter and area were calculated for a fiber bundle in a pultruded pellet.

The rheometer in use was based on the design of Giacomini [66,67](Figure 3.7). The SPR was heated by containing it within a convection oven, and the sliding plate was displaced by an Interlaken 3300 universal testing instrument. The rheometer has an effective surface area of $100 \times 230 \text{ mm}^2$. The gap thickness of the SPR was chosen to be 2 mm as the width of the fiber bundles falls below that gap size. A total deformation of 50 mm was chosen, as it is the maximum amount of deformation that still allowed for two sample plaques to be tested simultaneously. The velocity of the sliding plate was maintained constant throughout the experiment at a velocity of 20 mm/s, which equates to a shear rate of 10 s^{-1} .

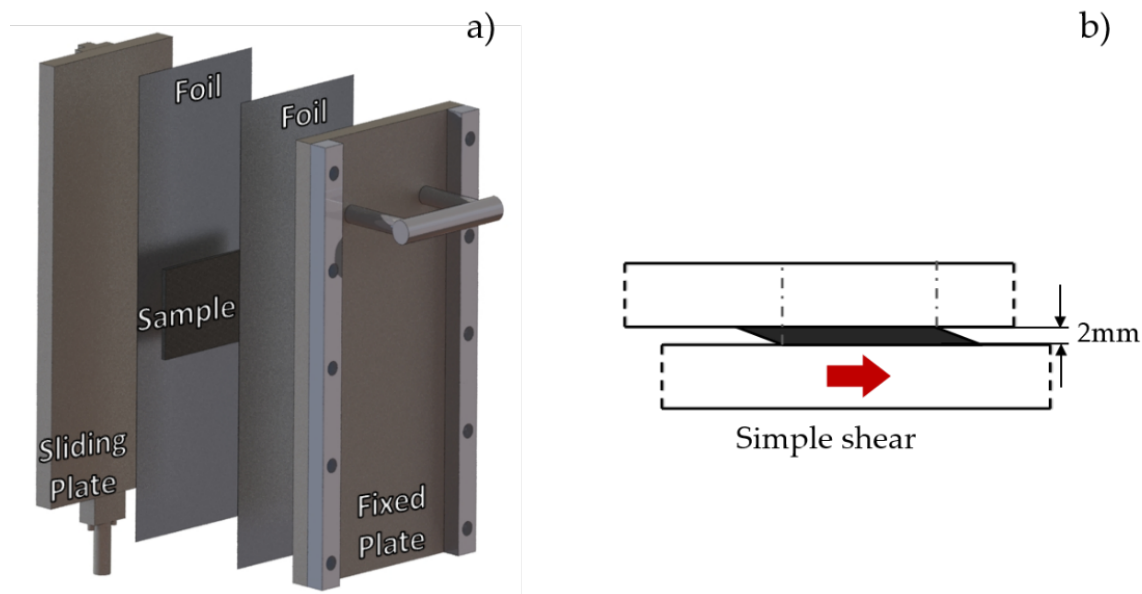


Figure 3.7: a) Layers of sliding plate rheometer (SPR). b) Side view of SPR with sheared sample

The experimental procedure used to properly implant and shear the samples was based on the experiments conducted by Simon [66]. The plates where the samples would be inserted were heated to the desired temperature, which gave both materials a viscosity of $576 \text{ Pa} \cdot \text{s}$. The sample plaques were then inserted into the sliding plate, where the straight edge of the plaques was colinear with those of the sliding plate in order to ensure that the pellets were perpendicular to the direction of displacement. Once the sample plaques were inserted and secured between the moving and stationary plates, the plaques were given time to reach and stabilize to the desired temperature. Once the desired temperature was reached, the plates were tightened to a gap of 2mm. Since the gap of the SPR was smaller than that of the initial sample plaque, the sample was slightly compressed to ensure full contact with the plates.

3.1.2 Dispersion Characterization

Once shear deformation has been applied, the heat of the SPR is turned off; the sample is removed once the apparatus's temperature has reached room temperature. Samples were then cut into rectangles to isolate the fibers of each pellet from the added

matrix of the plaque. They were then scanned using the μ CT Scanner to determine the position of the fibers after deformation. Figure 3.8 shows the fixture used to ensure the samples are vertical and separate from each other for every scan.

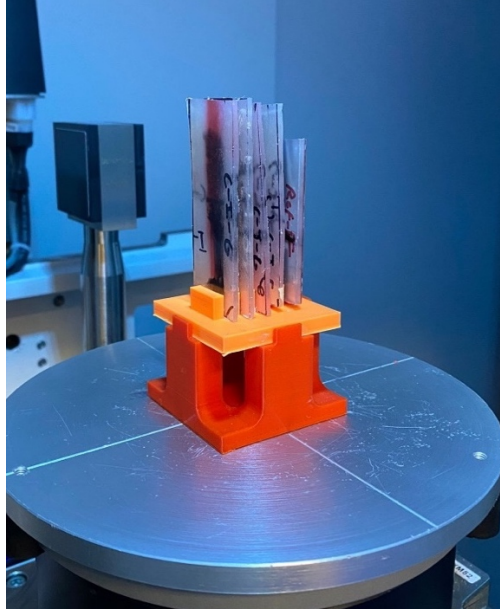


Figure 3.8: Mount used to scan samples with constant parameters.

The scans were then converted into lengthwise stack images to measure the fiber content along the direction of deformation. A color threshold is used to differentiate between fibers and matrix material. The number of pixels that are characterized as fiberglass is measured in every stack image (Figure 3.9). A voxel size of $40.96 \mu\text{m}/\text{pixels}$ was used during the scanning process. The voxel size then allows for the separation distance between each stack image to be known, which then allows for a fiber pixel weight distribution throughout a sample's length as shown by Figure 3.9. This allows for the range, concentration, and quantity of fibers to be measured along the length of the samples.

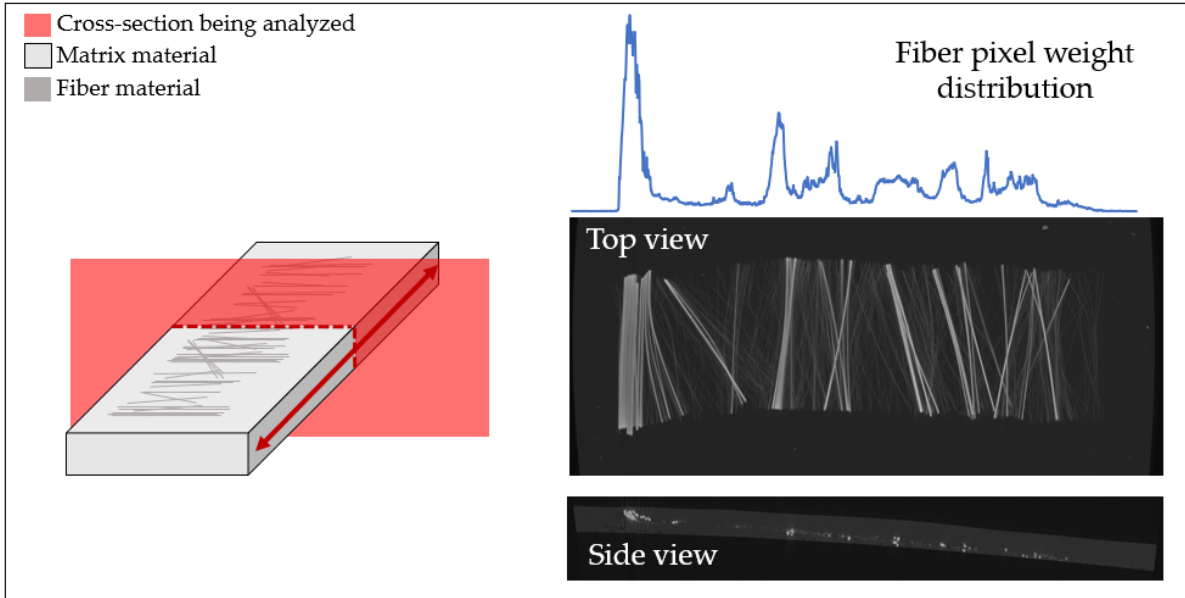


Figure 3.9: Method by which sheared sample was scanned and a fiber pixel weight distribution was calculated.

A histogram was made to depict the number of fiber pixels found throughout the length of the scan and allow for dispersion measurements to be done. When measuring dispersion, there are three common measurements used: range, Inter-Quartile Range (IQR), and standard deviation [68]. The range of the fibers was calculated by measuring the distance between the first and last fiber observed. While the range of the fibers' position is easy to measure and might be a useful metric for some applications, it is not a good metric for dispersion as it does not take material concentration into account. IQR is advantageous when measuring dispersion as it is not affected by extreme values that might skew the data. However, the most used value for dispersion is standard deviation [68]. Standard deviation measures the spread of the fibers' position, where a large standard deviation signifies a large spread of fibers in the sample. To measure the standard deviation of the fiber's position, equations 3 and 4 were used.

$$\bar{x} = \frac{\sum_{i=1}^{N_s} i \cdot vox \cdot N_f}{\sum_{i=1}^{N_s} N_f} \quad (3)$$

Equation 3 measures the mean position of the fibers, where N_s is the total number of stack images, vox is the voxel size that determines the real-life distance between stack images, N_f is the number of fiber pixels found in said stack image.

$$STDV = \sqrt{\frac{\sum_{i=1}^{N_s} (i \cdot vox - \bar{x})^2 \cdot N_f}{\sum_{i=1}^{N_s} N_f}} \quad (4)$$

Equation 4 is used to determine the standard deviation of the fiber's position. Where \bar{x} is the mean position of fibers calculated using equation 3.

3.1.3 Results

Results from the single-pellet dispersion study showed a combination of the erosion and rupture breakup mechanism, as seen in Figure 3.9. Dispersion for the single-pellet samples was evaluated based on the fibers' separation distance. The standard deviation was used to measure how dispersed fibers were on a sample to quantify dispersion. The results of standard deviation were plotted in comparison to the S parameter. A comparison between the coated and pultruded pellets can be seen below in Figure 3.10 All but two pultruded pellets were found to have a higher dispersion value, in terms of standard deviation, than all the coated pellets despite having similar S values. The trendlines also show that the S parameter has a more significant effect on the pultruded pellets than on the coated pellets.

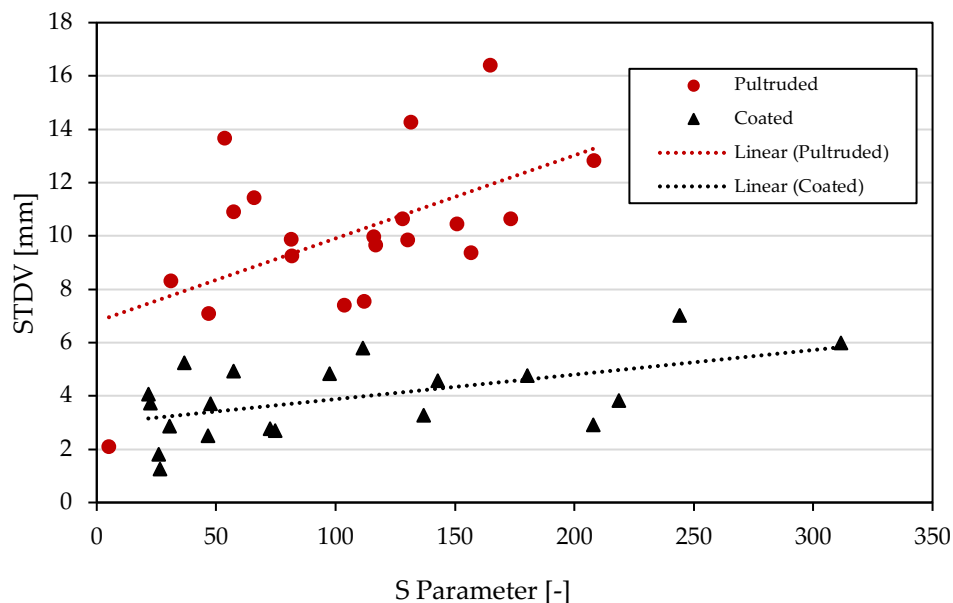


Figure 3.10: The standard deviation of the fibers' spread versus the S parameter calculated from the characterization process.

It should be noted that the experimental procedure employed in this study did not measure all possible morphological factors that could affect the dispersion rate. One of these parameters is the anisotropy of a bundle's shape. The anisotropy of a fiber bundle's cross-section could have a significant effect as fiber bundles aligned in a perpendicular direction, with respect to the direction of the deformation, would have a more considerable amount of separation than those aligned in a parallel direction. Gopalkrishnan [59] and Boyle[55] characterized the morphology of agglomerates using a measurement of filler concentration. However, when this value was calculated for both types of pellets, it was found to be very similar; therefore, it was not considered. Results show that the S parameter can gauge which pellets might lead to a larger dispersion rate based on the perimeter and area of a fiber bundle; however, the S parameter was unable to gauge this same dispersion rate when comparing two different types of LFT pellets.

3.2 Multi-Pellet Dispersion

To model the full dispersion model, fiber interactions will have to be considered using a multi-pellet system. Therefore, a multi-pellet filled system was studied using a Couette rheometer. The rheometer allowed for the isolation of parameters such as temperature, total deformation, residence time, and shear rate. Isolating these parameters allowed for a constitutive fiber dispersion model to be proposed. The experimental procedure was based on several experiments done at the Polymer Engineering Center [14,63,69]. The study done with the Couette rheometer had three objectives:

- i. Use experimental data to develop a dispersion measurement technique.
- ii. Characterize the fiber dispersion process.
- iii. Compare the dispersion process of pultruded pellets versus coated pellets.
- iv. Develop a time-dependent dispersion model.

3.2.1 Couette Rheometer

Fiber dispersion was studied for a multi-pellet filled system by subjecting the fiber-reinforced pellets to a simple shear flow using a Couette rheometer. The experimental setup was developed by the Polymer Engineering Center at the University of Wisconsin-Madison, as seen in Figure 11 [63,69]. The device depicted in Figure 3.11 is composed of two concentric cylinders with an annular gap where material plaques are placed. To guarantee no dispersion occurred before shearing the sample, the pellets were molten and slightly compressed into a 2mm thick rectangular cavity using a hot press. The small level of compression did not deform the bundles in a considerable manner. The plaques were then heated to 175°C in a convection oven and wrapped around the Couette's inner cylinder, as shown in Figure 3.12.a. The cylindrical sample and inner cylinder were then pressed into the outer cylinder employing an electric car jack, as shown in Figure 3.12.b. The result was a completely filled cavity with no air pockets. This procedure was

performed at temperatures well below melting, guaranteeing no damage or deformation was done to the bundles.

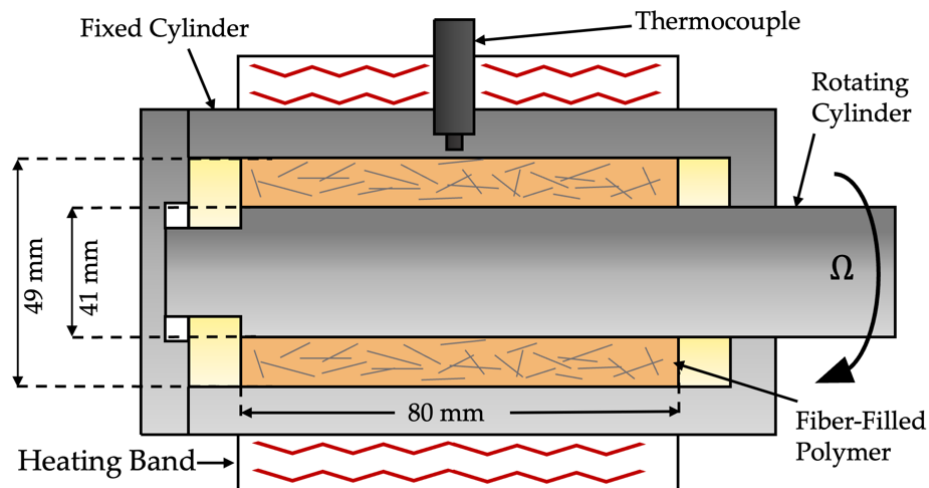


Figure 3.11: Schematic of Couette rheometer experimental setup.

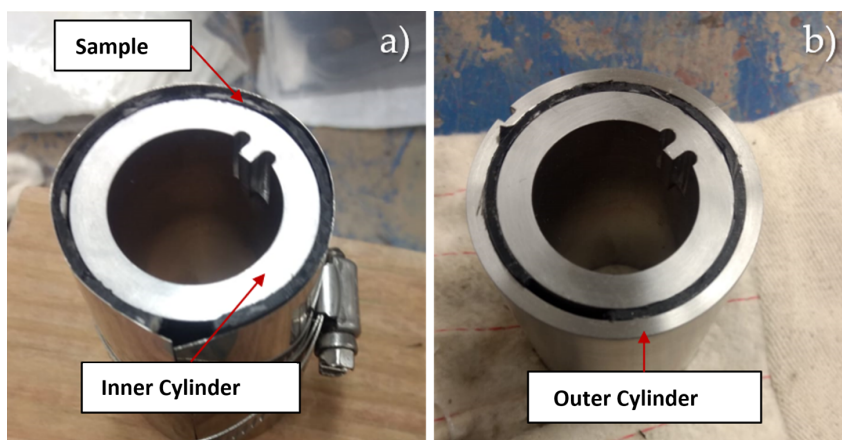


Figure 3.12: Sample preparation for Couette rheometer. Sample molding (a) and Couette after sample insertion (b)

The material is heated using a heating band that wraps around the device while a thermocouple is placed in the lengthwise mid-point to communicate with the heater controller. The outer cylinder is fixed while the inner cylinder rotates, creating a shear flow within the annular gap. The inner cylinder and heating band were controlled using a Brabender CWB/7.5 hp. The pellets are placed inside the gap between the cylinders with

an arbitrary orientation. Once the material has melted, it is secured by a combination of brass rings and two threaded lids.

Table 3: Couette rheometer experimental plan

Variables	Experiment 1	Experiment 2
Fiber content [%wt]	40	30
Melt temperature [°C]	250	210, 250
Rate of deformation [s^{-1}]	10	5, 10
Residence time [s]	5 to 30	5 to 30
Pellet type	Coated & Pultruded	Coated

Table 1 shows the parameters used in the Couette rheometer experiments. The first experiment was done to compare the dispersion mechanisms of coated pellets versus pultruded pellets. As shown in the single pellet dispersion study, pultruded pellets have a smaller diameter and a larger fiber-matrix surface interface which studies have shown leads to a larger dispersion value. Experiment 2 was done in order to characterize fiber dispersion behavior. This experiment allowed for the main drivers of dispersion to be known, as well as test potential dispersion models and characterize the cohesive stress of fibers. Once a deformation was applied, the material was cooled down to room temperature. The sample was then extracted using a hydraulic car jack to push the sample out of the outer cylinder. Samples are cut in half using a heated blade, then heated to 165 °C for 15 minutes and flattened using a press. Four 40 mm × 150 mm rectangles were extracted from each experiment.

3.2.2 Dispersion Characterization

The development of a dispersion measurement technique was crucial, as current techniques relied on subjective values [64,65] rather than quantifiable values, as explained in the state of the art section. For this objective, we developed a mathematical model using Excel where a color value is assigned to each pixel in an area, as shown in

Figure 3.13. This was done as preliminary samples were scanned using a μ CT and showed a similar trend to that of the mathematical model, as shown in Figure 3.14 below.

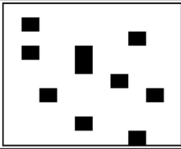
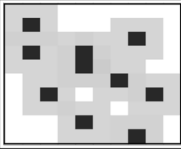
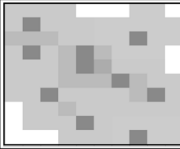

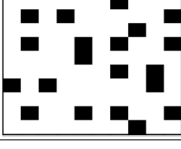



Examples	0% Dispersion	20% Dispersion	70% Dispersion	95% Dispersion
10% vf				
20% vf				

Figure 3.13: Mathematical representation of the dispersion process.

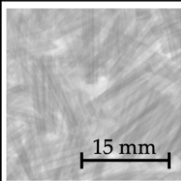
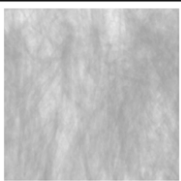


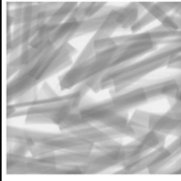

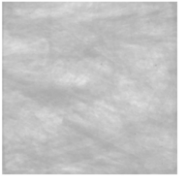

Material \ Residence Time	0 sec	5 sec	30 sec	300 sec
Pultruded				
Coated				

Figure 3.14: Preliminary scans of Couette rheometer experiments

By measuring the standard deviation of the pixel's grayscale values, we can determine the homogeneity of a sample and, therefore, its dispersion value. However, when measurements were taken of undispersed samples, it was noticed that the standard deviation measurements were different despite being made of the same material and using the same manufacturing technique. As shown in Figure 3.15, by using the mathematical model, it was determined that different fiber volume fractions had different values of standard deviation. Therefore, if the area that is being scanned does not contain the exact amount of filler percentage it will have a different standard deviation. As a result, the Coefficient Of Variation (COV) (Equation 5) was used as the

measure of homogeneity as it normalizes the standard deviation based on the amount of filler material in the scanned area.

$$COV = \frac{\text{Standard Deviation}}{\text{Mean Gray Value}} \quad (5)$$

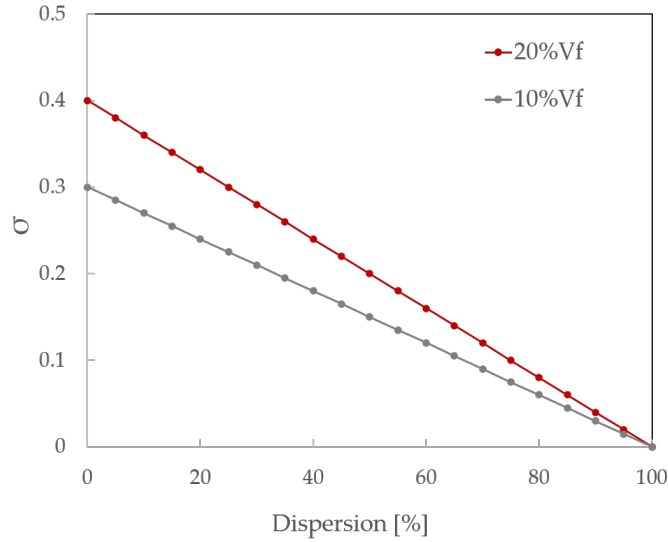


Figure 3.15: Standard deviation with respect to different volume fractions

Once a COV value was calculated for each sample, including the undispersed and fully dispersed samples, equation 6 was used to calculate the dispersion value of the samples, where ε is the dispersion value.

$$\varepsilon = \frac{COV_{\text{Sample}} - COV_{0\% \text{ sample}}}{COV_{100\% \text{ sample}} - COV_{0\% \text{ sample}}} \quad (6)$$

Figure 3.16 shows how equation 5 gives a value of dispersion in terms of percentage based on the COV values of the reference points. Therefore, it is important to note that the results shown by this study rely on the reference points, and results may vary for other studies if different reference points are used. For the 0% reference, to guarantee no dispersion occurred before scanning the sample, pellets were molten and slightly compressed into a 2mm thick rectangular cavity. The small level of compression did not deform the bundles in a considerable manner. For the 100% reference, the material

was sheared in the Couette rheometer for 300 seconds at a shear rate of 10 s^{-1} , resulting in a total strain of 3000.

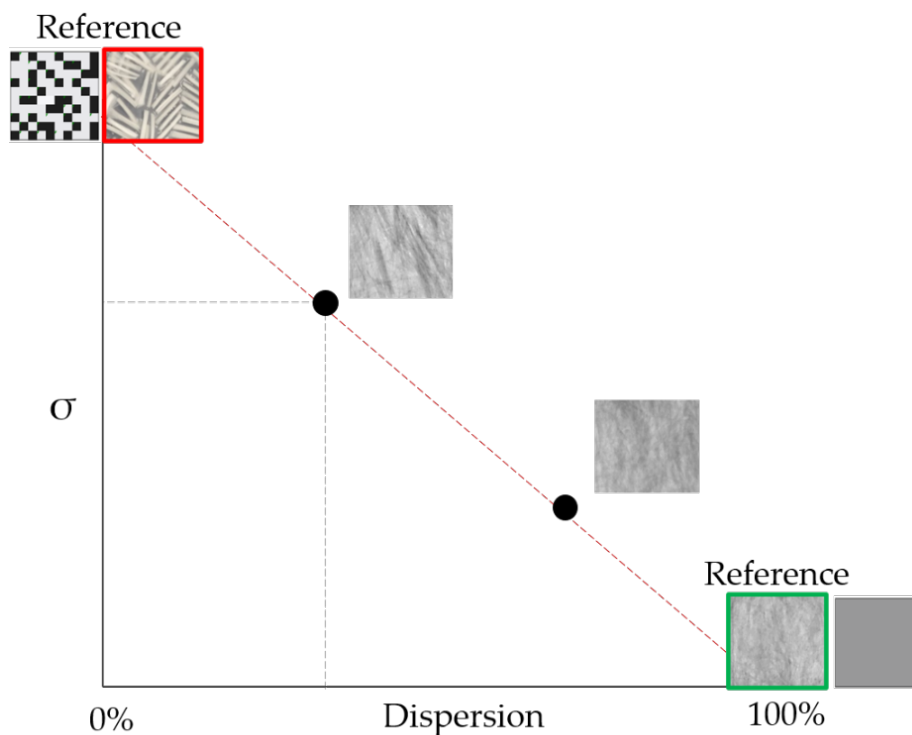


Figure 3.16: Linear relationship between standard deviation and dispersion value.

It was also noted during the analysis that the dispersion value would be altered depending on the size of a region. Therefore, a region of interest (ROI) study had to be done to ensure the proper number of pixels was being taken into account for the dispersion measurement. Figure 3.17 shows the sample that was used to study the effect of the ROI size and its effect on the variation of COV. The ROI study showed that levels of variation will decrease as the sample size becomes larger. Therefore, it is always required to scan the largest amount of area possible. Figure 3.18 shows how the largest possible sample from the Couette rheometer was scanned along with the reference samples.

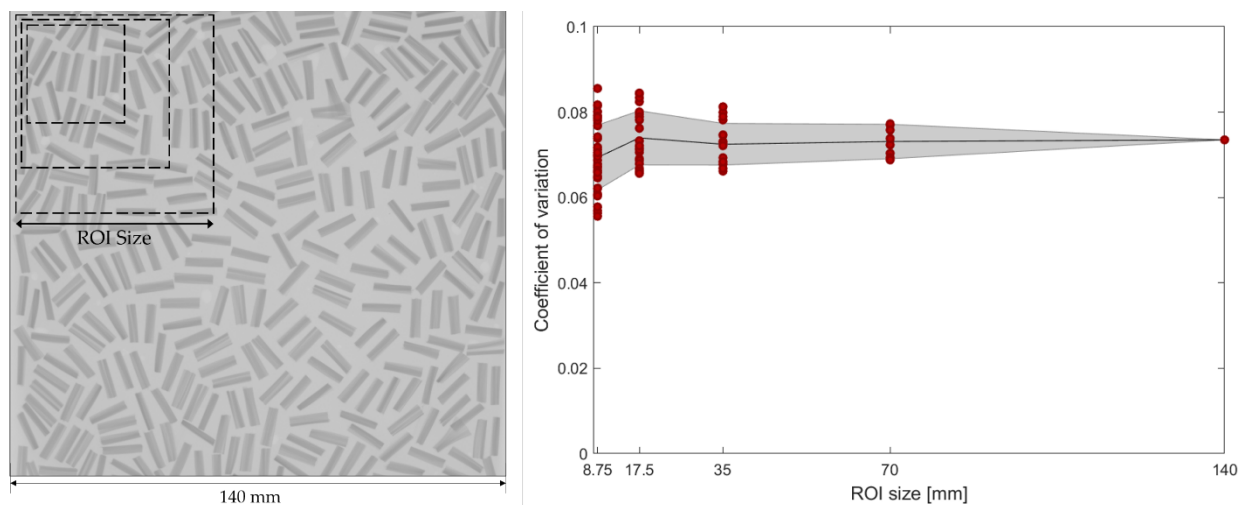


Figure 3.17: ROI study determining variation with respect to ROI size.

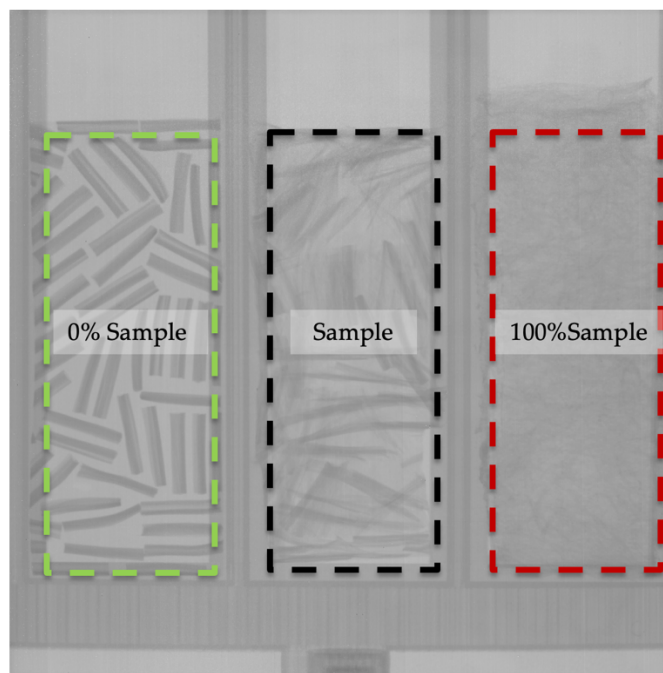


Figure 3.18: Sample scan of test sample with 0% and 100% dispersed samples.

3.2.3 Results

Results from experiment 1 are shown in Figure 3.19 below. A comparison of dispersion behavior between coated and pultruded pellets was done. Results from experiment 1 line up with the literature on agglomerate dispersion, where the rate of dispersion will be similar regardless of the size of the agglomerate or shape [52,54,57,62]. This can be seen

in Figure with the graph showing dispersion values using their own individual reference points. However, when dispersion was measured using the same 0% and 100% reference points, pultruded pellets seemed to already have an initial dispersion value. This can also be seen in Figure 3.19, where the 0% reference of the pultruded pellets is already more dispersed than the 0% reference of the coated pellets.

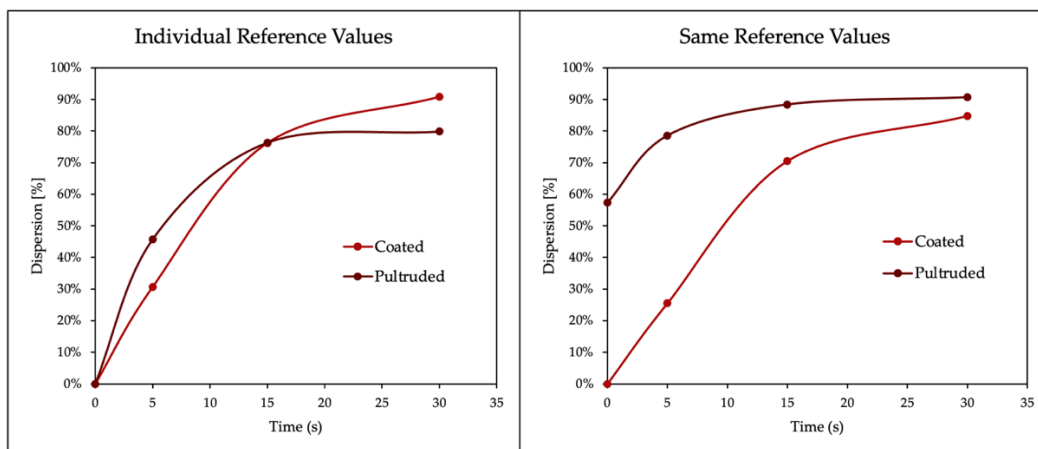


Figure 3.19: Dispersion results comparing coated pellets with pultruded pellets

Results from experiment 2 can be seen in Figure 3.20 below, showing how, at equal deformation values, dispersion tends to follow a similar trend as described by Manas-Zloczower [52,54]. However, the effect of shear stress cannot really be observed from these results as the experiments done at 210 °C should have differed by some degree as the material at a shear rate of 10 s⁻¹ has a higher total shear stress. Using these same results, critical stress was calculated, as shown by Manas-Zloczower[52,54,58] in Figure 3.21. Critical stress was found to be between 5 kPa, and 7.9 kPa, which averaged comes to 6.48 kPa.

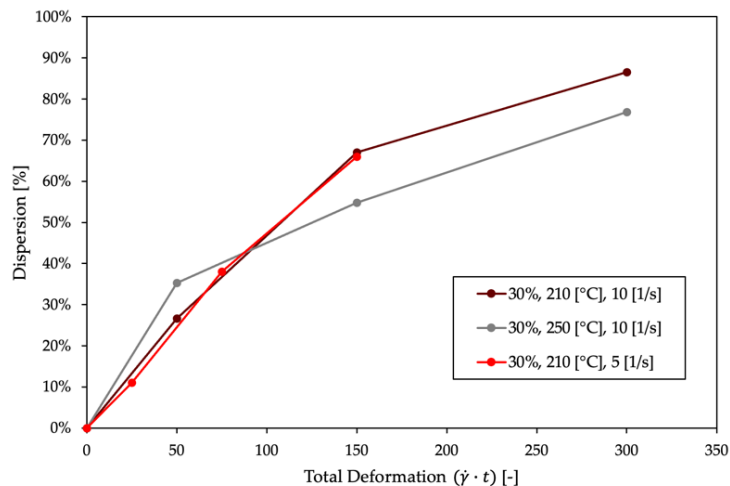


Figure 3.20: Dispersion with respect to total deformation for several experiments.

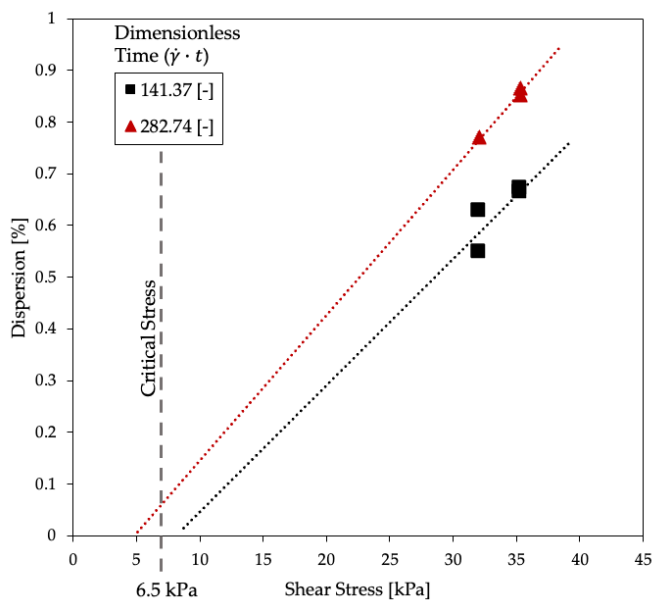


Figure 3.21: Linear regression showing the critical stress of fiber agglomerates.

3.3 Modeling Fiber Dispersion for Couette Rheometer

Using the agglomerate model described by Manas-Zloczower[52,54] as the starting point for the fiber dispersion model (Equation 7), where the $\dot{\gamma}$ is the shear rate, t is the residence time, and k is a fitting parameter.

$$\varepsilon = 1 - e^{-k \cdot \dot{\gamma} \cdot t} \quad (7)$$

A term is introduced into the model, which is the ratio of the hydrodynamic shear stress (τ) and critical stress (σ_c) raised to a power (n) (Equation 8).

$$\varepsilon = 1 - e^{-k \cdot \dot{\gamma} \cdot (t-t_o) (\tau/\sigma_c)^n} \quad (8)$$

Where the shear stress is calculated using equation 8. Where the dynamic viscosity (η) is a function of shear rate ($\dot{\gamma}$) and temperature (T).

$$\tau = \eta \frac{dv_z}{dy} = \eta(\dot{\gamma}, T) \cdot \dot{\gamma} \quad (9)$$

This term allows for the mechanism of erosion and breakage to be introduced into the equation without using two separate models for each mechanism. By fitting the model to Couette rheometer data, n was determined to have a value of 0.5 from equation 7, resulting in the model proposed shown in equation 10. For this set of experiments, k was found to be 0.0032.

$$\frac{\partial \varepsilon}{\partial t} = k \dot{\gamma} (\tau/\sigma_c)^{0.5} \cdot e^{-k \cdot \dot{\gamma} \cdot (t-t_o) (\tau/\sigma_c)^{0.5}} \quad (10)$$

The model comparison with Couette rheometer data is shown in Figure 3.22. The model shows a good fit with the experimental data. This model was then used to predict dispersion in a single screw extruder, which will be shown later in the report.

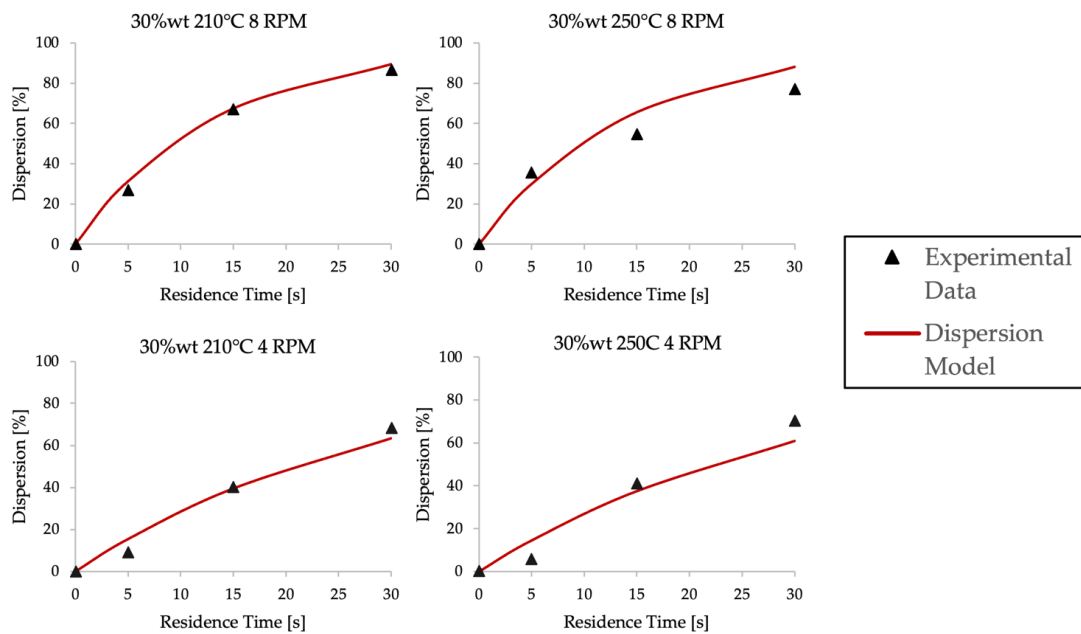


Figure 3.22: Comparison between the dispersion model and experimental data.

4. Modeling Fiber Dispersion in Single-Screw Extruder

4.1 Screw Pull-out Experiments

In order to validate the dispersion model for a single screw extruder, screw pull-out experiments were done. With the dispersion measurement technique developed, it was now possible to accurately measure the dispersion process within a screw in terms of screw position. Figure 4.1 illustrates a single screw extruder during the process of a screw pull-out experiment where preliminary scanned samples are shown at different positions in the screw. The position of the screw is measured in terms of the ratio of the length of the screw (L) over the diameter of the barrel (D), where an L/D of 0 represents the position at the hopper and an L/D of 30 represents the position at the die of the screw.

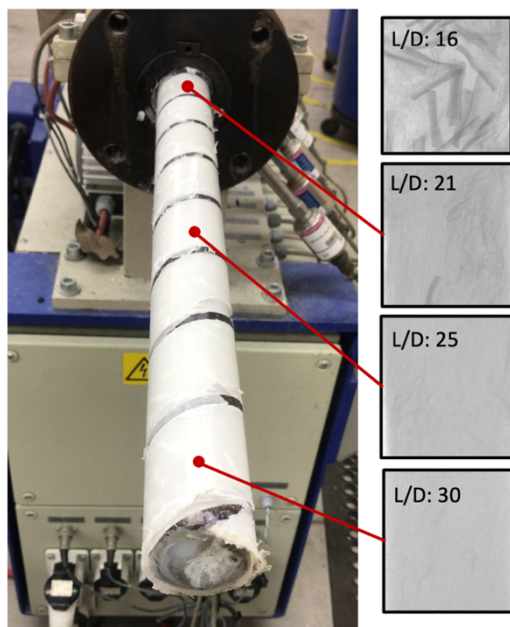


Figure 4.1: Preliminary results from screw pull-out experiments

Figure 4.2 shows a visual representation of the single screw extruder used and modeled for this study. The temperature of the barrel is controlled by four band heaters, which will be represented by their temperature profile; for example, “250-220 °C” means

the first band heater near the hopper was set to 250°C and the following band heater was set to 240°C and so on, until reaching 220°C. Table 4 shows the rest of the screw's dimensions and process parameters used in this study.

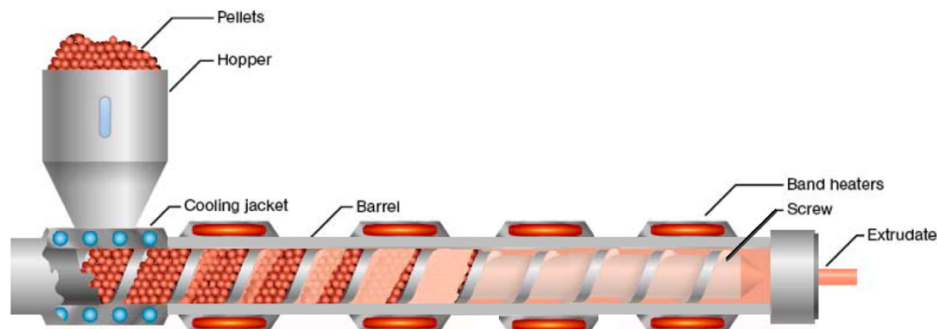


Figure 4.2: Visual representation of single screw extruder used for this study.

Table 4: Screw Pull-out experimental parameters

Experimental Parameters	Values
Screw Length	1.35 [m]
Screw Diameter	45 [mm]
Initial and Final Channel Height	7, 2.8 [mm]
Channel Width	31 - 49 [mm]
RPM	15, 30, 60 [RPM]
Fiber Content	30%, 40%[wt]
Material Melting Temperature	178 [°C]
Pellet Length	15 [mm]
Pellet Diameter	2, 3 [mm]
Heating Profiles	250-250-250-250[°C] 250-240-230-220[°C] 190-200-210-220[°C]

The first step of the experimental procedure is to run the single screw extruder with a set of given parameters from Table 4. After the extruder has maintained a steady state for 10 minutes, the screw is stopped as quickly as possible, which would take 2 seconds to come to a full stop. Once the material had solidified and reached room

temperature, the barrel was heated to a temperature of 165 °C in order to begin the screw pull-out procedure. After the entire screw was pulled from the barrel, numerous samples were extracted along the length of the extruder screw. One sample was taken from each screw rotation, also referred to as pitch. An extracted sample was then flattened by heating the material at 165 °C and compressing it with a press at low pressures. This flattening procedure was based on studies done by the Polymer Engineering Center [14,63]. The flattened sample was then scanned and measured for dispersion using the same methodology as the multi-pellet dispersion study. This procedure is illustrated in Figure 4.3.

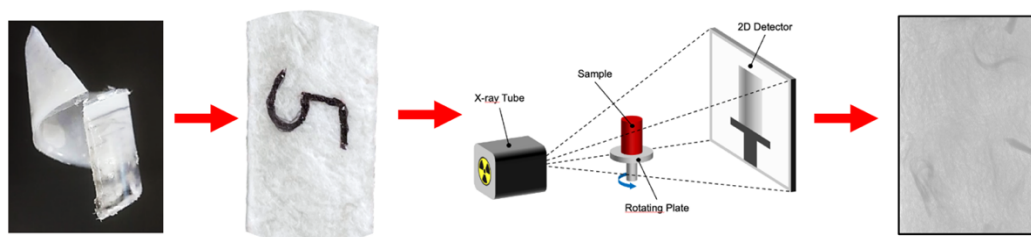


Figure 4.3: Procedure to scan extracted samples from screw.

The results of this study are shown in a series of figures below. Figure 38 shows the effect of the barrel temperature profile. It shows that dispersion is delayed as the initial temperature is lower. This can be explained as the material takes a longer time to melt, and therefore, fiber bundles do not disperse. Figure 4.4 also shows how, even when melting is delayed, a high dispersion can be achieved due to a large viscosity near the melt front. Error bars in Figures 4.4 and 4.5 indicate range of samples.

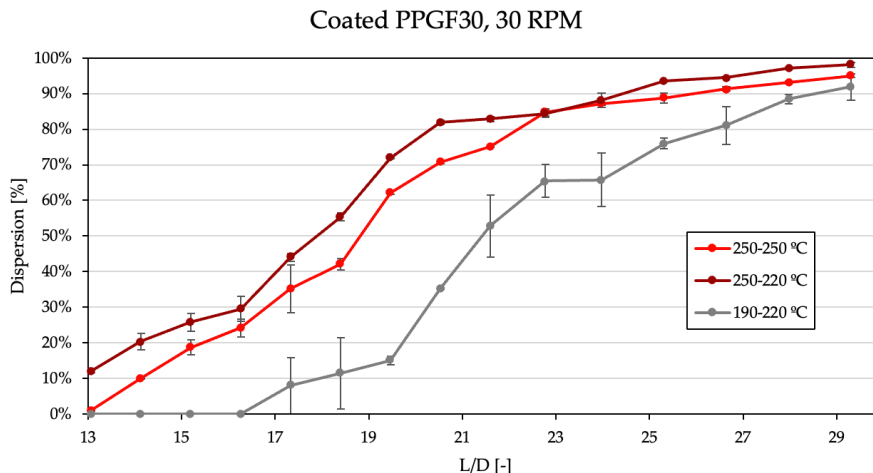


Figure 4.4: Dispersion results comparing different barrel temperature profiles.

Figure 4.5 compares three different RPMs with the same heating profile. Because the material flows slower at lower RPMs, the material can melt at a lower position in the screw which cause the dispersion process to occur much sooner. Similar to the previous results, even when melting is delayed, as seen for results of 60 RPM in Figure 4.5, high levels of dispersion are achieved due to the high shear stresses. Results for 15 RPM also indicate that reaching a high level of dispersion early is not very advantageous in a long screw as dispersion seems to reach a plateau as its dispersion was only increased by 15% from an L/D_B of 20 to 29.8.

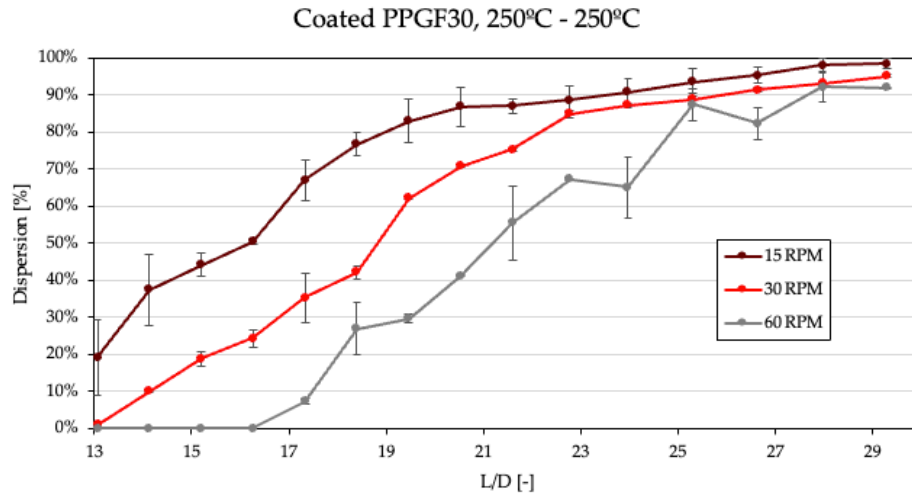


Figure 4.5: Dispersion results comparing three screw velocities.

Figure 4.6 shows the effect of fiber content while maintaining temperature and RPM constant. Results from Figure 4.6 are difficult to explain, as a higher level of fiber content makes the overall thermal conductivity of the material higher and, therefore, should have melted at a more initial position. Finally, Figure 4.7 compares pultruded pellets with coated pellets using the same process parameters. Like the Couette rheometer results in the previous study, pultruded pellets initiated with a degree of dispersion higher than that of pultruded pellets; however, both materials reached a similar level of dispersion for this study. These results were later used for the validation of the dispersion model discussed in the following section.

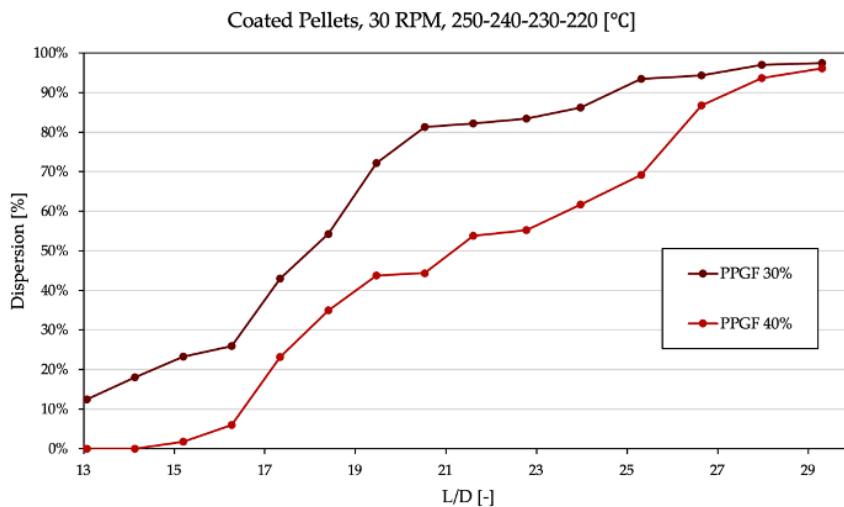


Figure 4.6: Dispersion comparison of materials with different fiber content.

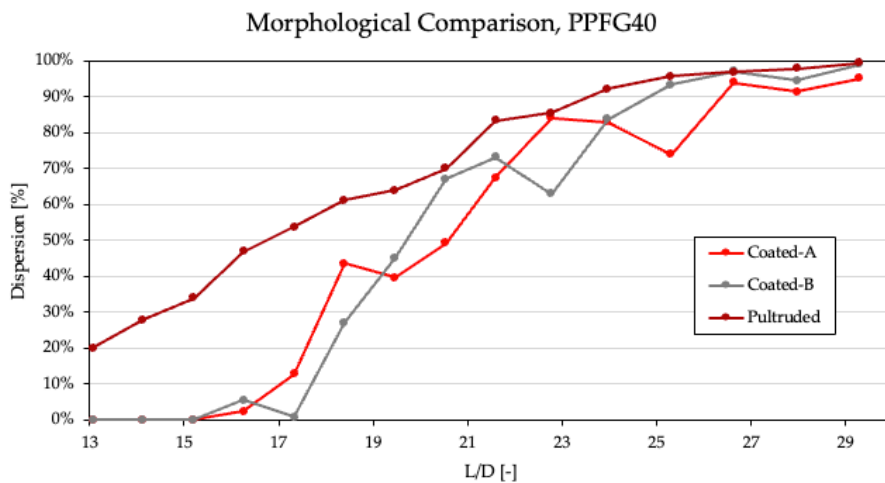


Figure 4.7: Dispersion comparison between pultruded pellets and coated pellets.

4.2 Modeling Single Screw Extruder

In order to determine the melting process during plasticizing, one of Tadmor's melting models was implemented. The melting model used is a non-Newtonian model that considers the curvature of the screw by using the average channel width[31–33]. The melting model does not consider the temperature of the screw and regards the screw surface as a zero-heat flux surface. The melting rate, Φ , is calculated for a non-newtonian polymer using equation 11 below. Where V_{bx} is the velocity of the barrel in the x-direction, ρ_m is the density of the melt polymer, k_m is the thermal conductivity of the melt, T_b is the barrel temperature at that section, T_m is the melting temperature of the polymer, T_s is the temperature of the solid polymer at the entrance of the screw which was assumed to be 23°C, c_s is the specific heat, λ^* is the heat of fusion of the polymer, U_1 and U_2 are material properties based from the power law model of viscosity.

$$\Phi = \left\{ \frac{V_{bx} U_2 \rho_m [k_m (T_b - T_m) + U_1 / 2]}{2 [c_s (T_m - T_s) + \lambda^*]} \right\}^{1/2} \quad (11)$$

As the screw used for this study has three sections, two constant depth channel sections, and one tapered channel section, two different types of solid bed profile models had to be used. The solid bed profile model for a constant depth channel is shown in equation 12. Where X is the solid width, \overline{W}_o is the average width of the screw channel, G indicates the volumetric flow rate, H_o is the screw channel height at which melting began, H is screw channel height in that section, and z indicates the helical length position of the screw.

$$\frac{X_2}{W_2} = \frac{X_1}{W_1} \left(1 - \frac{\Phi \overline{W}_o H_o}{2 G X_1^{1/2} H} (z_2 - z_1) \right)^2 \quad (12)$$

The solid bed profile model used for the tapered section of the screw is shown below in Equation 13.

$$\frac{X_2}{W_2} = \frac{X_1}{W_1} \left(\frac{\psi}{A} - \left(\frac{\psi}{A} - 1 \right) \left(\frac{H_1}{H_1 - AZ_2} \right)^{1/2} \right)^2 \quad (13)$$

where

$$A = \frac{H_o - H_F}{z_T} \quad (14)$$

$$\psi = \frac{\Phi W^{1/2}}{(G/H_o)} \quad (15)$$

Equation 14 indicates the slope of the tapered section where H_o is the initial screw channel height at the beginning of the tapered section, H_F is the final channel height, and z_T is the total helical length where the height changes. Equation 15 indicates the ratio of the rate of melting per unit down the channel distance to the rate of mass flow of solids per unit channel depth. Combining equations 10-14 gives the total solid width of the channel with respect to the helical distance.

Figure 4.8 shows how the transition from solid to a fully melted state in terms of the solid (X) to width (W) ratio. The volumetric flow rate, G , was measured experimentally from screw pull-out experiments. This melting will not be used to calculate dispersion but will be used to determine where dispersion begins to occur. Once the dispersion is determined to begin, the material within the screw will be considered fully melted. Equations of motion will then be used to determine shear rate, shear stress, and total deformation.

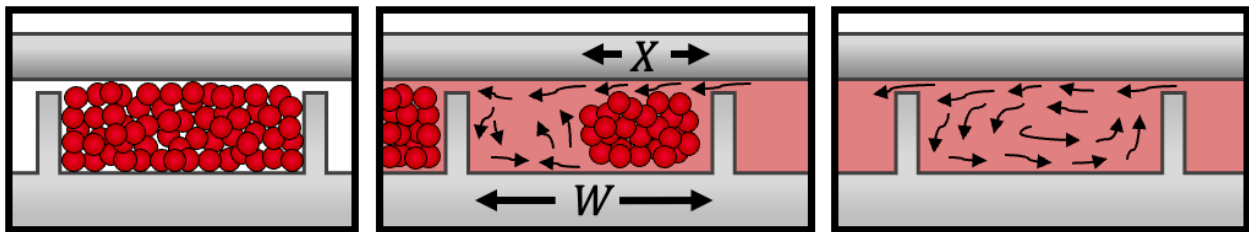


Figure 4.8: Left) the material begins as a solid in the screw channel, Middle) solid to melt transition where solid width (X) is compared to channel width (W), Right) fully melted state.

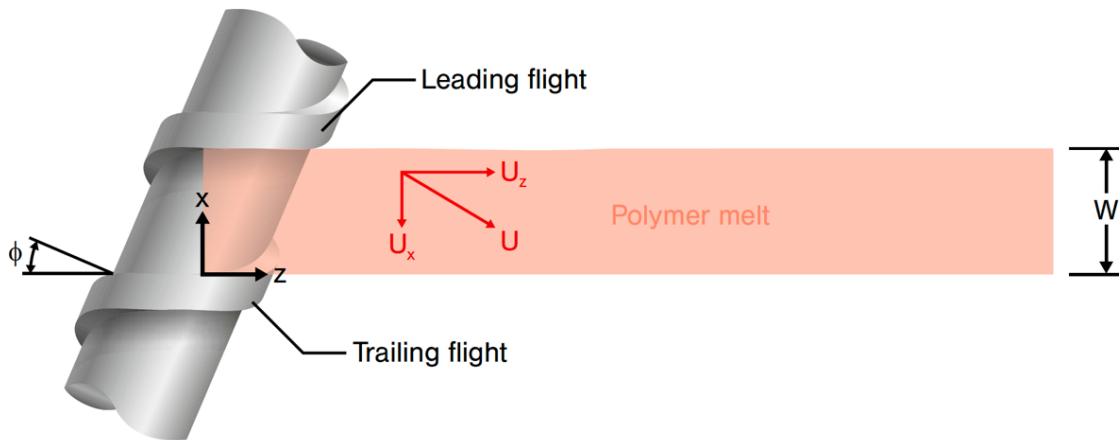


Figure 4.9: Visual representation of material system modeled as a rectangular prism unwinding from the screw.

Modeling a single screw extruder can be simplified by unwinding the material system into a long rectangular geometry that depicts the screw channel, as shown in Figure 4.9 [25]. This assumption works when equation 16 is satisfied. While the equation does not satisfy the entire screw, it only has to satisfy the section where dispersion will be calculated, and previously explained, it will happen once a critical melting point occurs. The second assumption that is needed to determine the overall deformation is to assume the channel is shallow with respect to the screw diameter. To assume the screw channel can be considered shallow, equation 17 has to be satisfied where R_b is the barrel radius and R_s is the radius of the barrel minus the channel height.

$$\frac{H}{D_b} < 0.1 \quad (16)$$

$$\frac{R_b}{R_s} < 0.1 \quad (17)$$

Figure 4.10 demonstrates where both the shallow channel assumption and neglect of curvature hold true for the screw position. Because the width of the screw channel is much larger than its height, the assumption of neglecting end wall effects holds true [25,48,50]. For the tapered section of the screw, the lubrication approximation will also be taken into account as the channel height changes very slowly with respect to the helical length []. Modeling the flow inside of a screw is very difficult due to the geometry

of a screw channel and the nature of the equations of motion. As a result, the following assumptions were made in order to model the flow within a screw:

- A Newtonian fluid is assumed for the equations of motion.
- The flow in the x-direction is assumed to be negligible due to the large width of the channel.
- Viscous heating is not considered for the dispersion model, only for the melting model.
- While channel depth changes throughout the length of the screw channel, the effects from this aspect on pressure and y-direction velocity will be neglected as the channel depth changes very slowly.

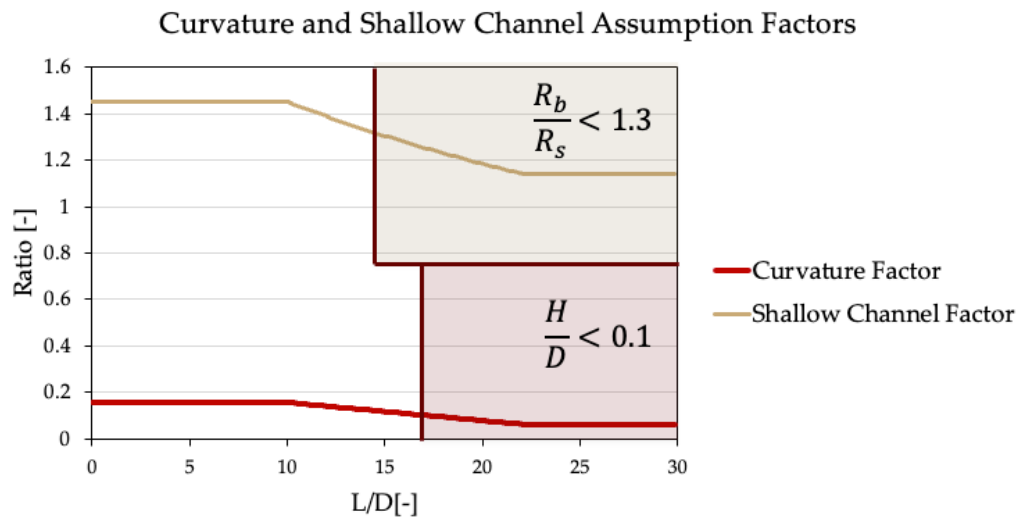


Figure 4.10: Graph of curvature factor and shallow channel factor determining where assumptions hold throughout the length of the screw.

The screw length used for this study is of 1.35 meters and the helical length is of 4.37 meters. It will also be assumed that the barrel is rotating instead of the screw, as this has been shown to be a valid assumption and simplifies the modeling aspect [25,31–33,39,40].

4.3 Modeling Fiber Dispersion

After comparing the melting model with the screw pull-out experiments, it was found that dispersion begins when the solid-width ratio is near 0.6. Figure 4.11 illustrates how the last dispersion value of 0% is near the location where the solid width ratio has a value of 0.6. Therefore, once the solid width ratio has reached 0.6, the dispersion calculation initiates.

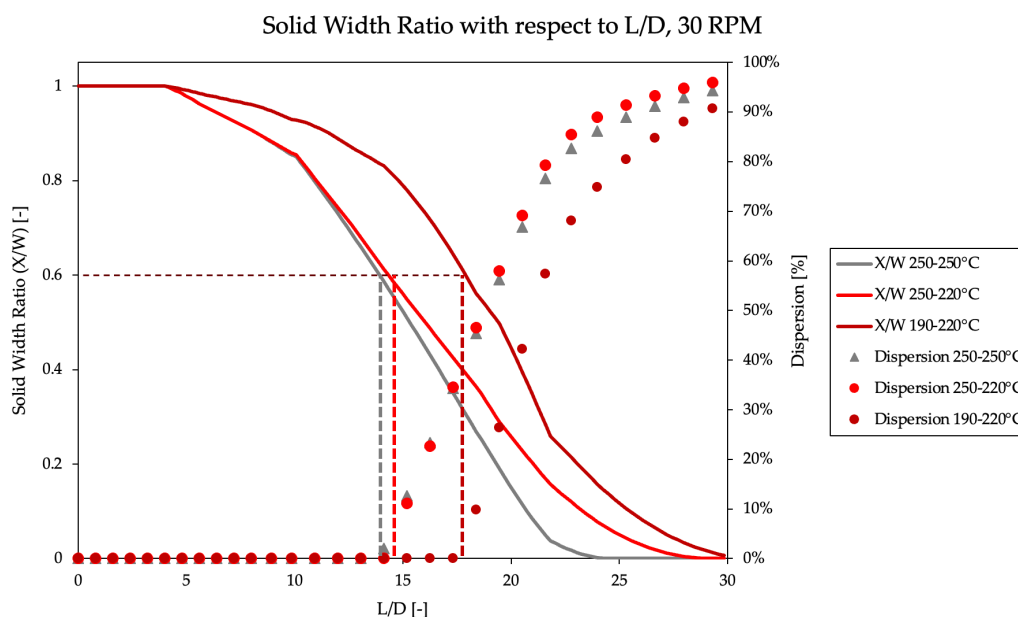


Figure 4.11: Solid width ratio plotted along with dispersion values, showing dispersion begins to occur near the position where the solid width ratio is 0.6.

The assumption that fiber dispersion begins to occur when the solid/melt width ratio is 0.6 was also found by using a micro-CT scanner to scan the samples in the screw. Figure 4.12 shows the samples taken at different positions lined up continuously; average dispersion values are also mentioned in the figure.

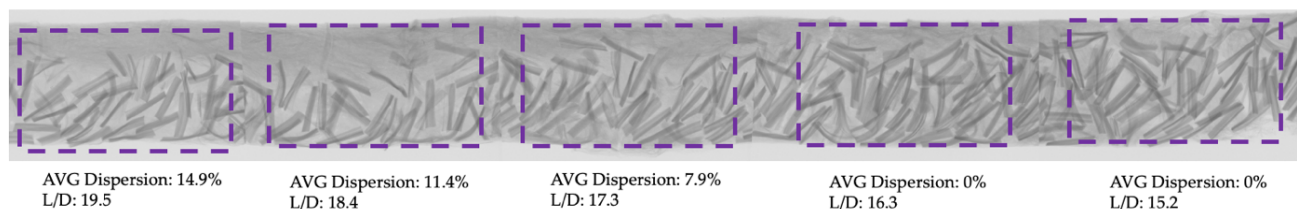


Figure 4.12: Samples from the screw pull-out experiment (30 RPM, 190-220°C) lined up continuously to show dispersion evolution.

Once the images of the samples were lined up, a clear thin section was noticed to have a higher level of dispersion than the rest of the sample. Figure 4.13 shows the area where there is a clear distinction between high dispersion and low dispersion. It also shows where the solid/melt interface is calculated to be. The modeled melt/solid interface lines up with the area in which dispersion is much higher. Towards an L/D of 19.5, the solid/melt interface deviates from the dispersed film; this could be that dispersion has already occurred within the melt film but is not clearly visible to the naked eye.

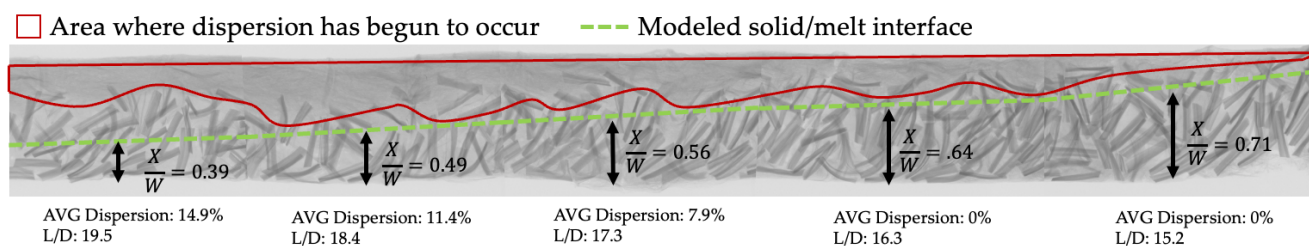


Figure 4.13: Samples from the screw pull-out experiment (30 RPM, 190-220°C) lined up continuously to show the solid width ratio with respect to dispersion.

Figure 4.13 shows a visual representation of the model. Where the top wall acts like a sliding plate and the bottom plate remains fixed, where $H(z)$ is the distance separating the plates, V_{Bz} is the barrel velocity with respect to the z -direction, and L_ε represents the distance from the position where the solid-width ratio is 0.6 and the end of the screw. This method of modeling a single screw extruder is based on studies, and models, done by Osswald [48] and Tadmor [31,32]. In combination with the previously stated assumptions, if the following assumptions are also made:

- i. Steady-state flow.
- ii. Laminar flow.
- iii. Fully developed flow.
- iv. Fluid is incompressible.
- v. No slip at walls.

vi. Gravity is neglected.

The equations of motion simplify to Equations 18 and 19 below. These equations have analytical solutions and can be used to predict melt velocity profile, shear rate, and pressure throughout the screw.

$$\frac{\partial P}{\partial x} = \mu \frac{\partial^2 v_x}{\partial y^2} \quad (18)$$

$$\frac{\partial P}{\partial z} = \mu \left(\frac{\partial^2 v_z}{\partial x^2} \right) \quad (19)$$

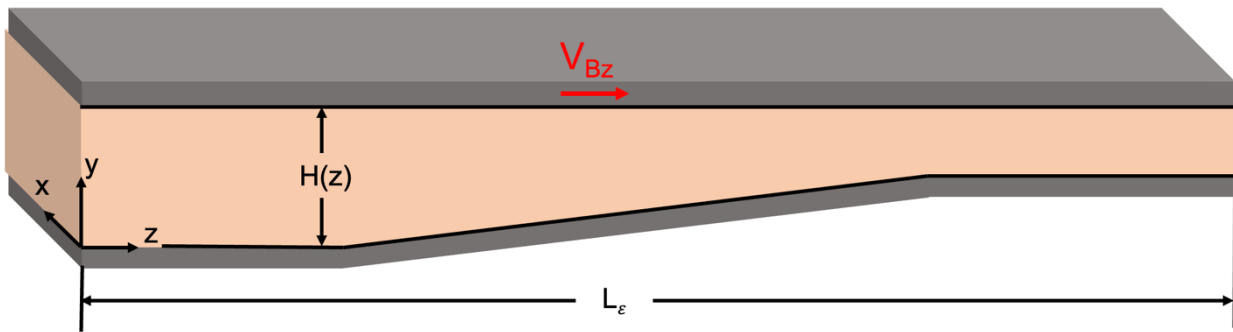


Figure 4.14: Visual representation of the method used to model screw channel where the barrel (Top) surface acts as a sliding wall and the screw (Bottom) surface acts as a fixed wall.

As it was shown in the multi-pellet dispersion study and by various studies done under Manas-Zloczower[52,54,57], in simple shear flow, total deformation is the main driver of dispersion. However, the dispersion model shown in Equation 10 relies on residence time and shear rate. To simplify this approach, total deformation will be calculated as an average through channel length position. The shear rate will be calculated using equation 20 to approximate the total deformation in the screw channel, as shown by Tadmor [31,32].

$$\dot{\gamma} = \frac{dV_{bz}}{dy} = \frac{V_{bz}}{H} \left[1 + 3 \frac{Q_p}{Q_d} \left(1 - 2 \frac{y}{H} \right) \right] \quad (20)$$

By measuring the shear rate at the mid-plane between the barrel surface and the screw surface, we simplify the shear rate into Equation 21.

$$\dot{\gamma} = \frac{V_{bz}}{H} \text{ at } y = \frac{H}{2} \quad (21)$$

Using the barrel's velocity in the z-direction multiplied by the time gives the total deformation in terms of the z-direction position, as shown by equation 22.

$$\gamma = \dot{\gamma} \cdot t = \frac{V_{bz}}{H(z)} \cdot t = \frac{z}{H(z)} \quad (22)$$

By substituting equation 22 into the time dependent model from equation 10. A position dependent dispersion model is made, shown in equation 23.

$$\varepsilon = 1 - e^{-k \cdot \frac{(z-z_0)}{H(z)} (\tau/\sigma_c)^{0.5}} \quad (23)$$

The model is then implemented into a 1D model where viscosity is dependent on barrel temperature and shear rate measured at that position by equation 23. The shear rate is calculated by equation 21. The fitting parameter k is changed to 9e-5 from 24e-4 of the Couette dispersion model. Cohesive stress remains the same from the previous study.

4.4 Validation of Fiber Dispersion Model

Results for the dispersion model are shown in a series of figures below. The modeled results are graphed with the addition of the experimental values measured from the screw pull-out experiments. All dispersion models are done using the same parameters.

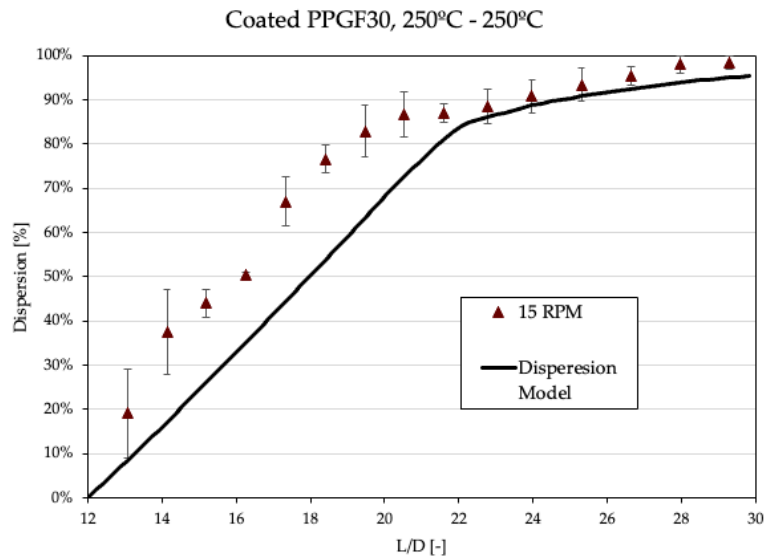


Figure 4.15: Comparison between Experimental data and model for (15 RPM, 250-250°C, PPGF30).

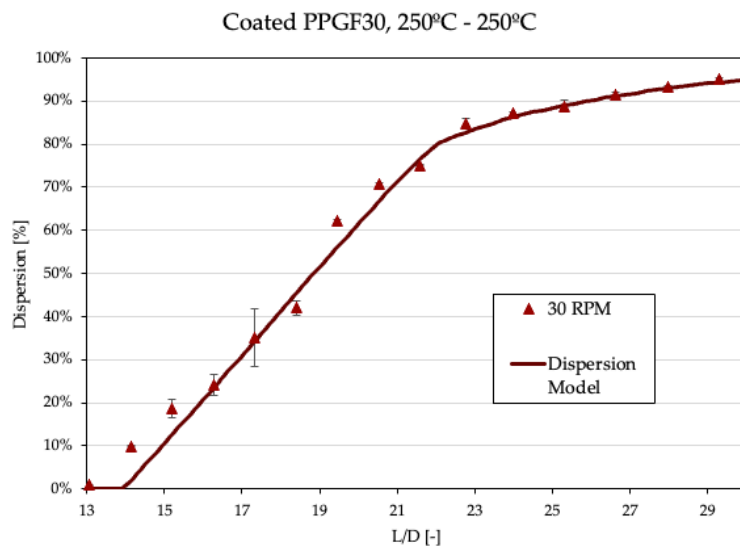


Figure 4.16: Comparison between Experimental data and model for (30 RPM, 250-250°C, PPGF30)

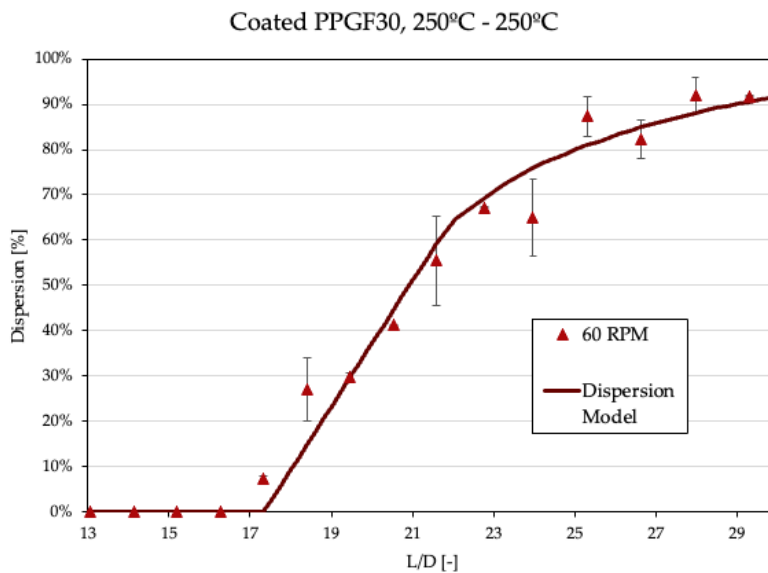


Figure 4.17: Comparison between Experimental data and model for (60 RPM, 250-250°C, PPGF30)

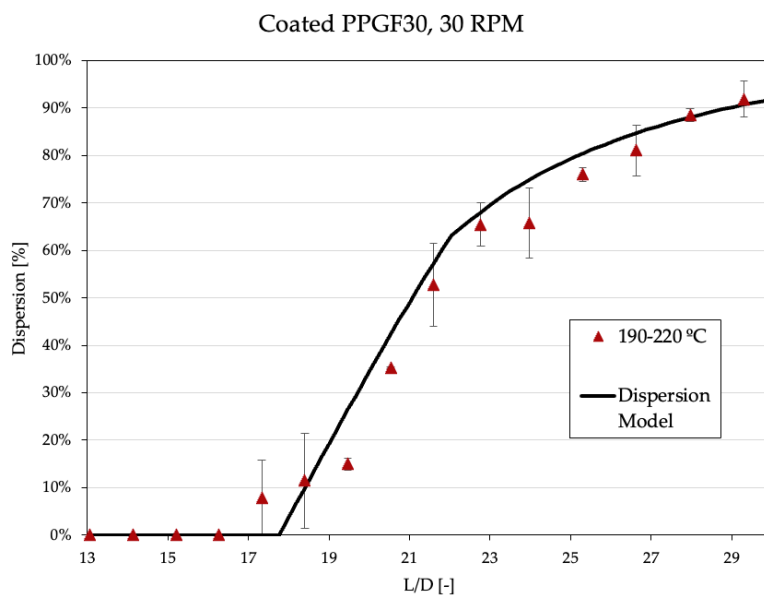


Figure 4.18: Comparison between Experimental data and model for (30 RPM, 190-220°C, PPGF30)

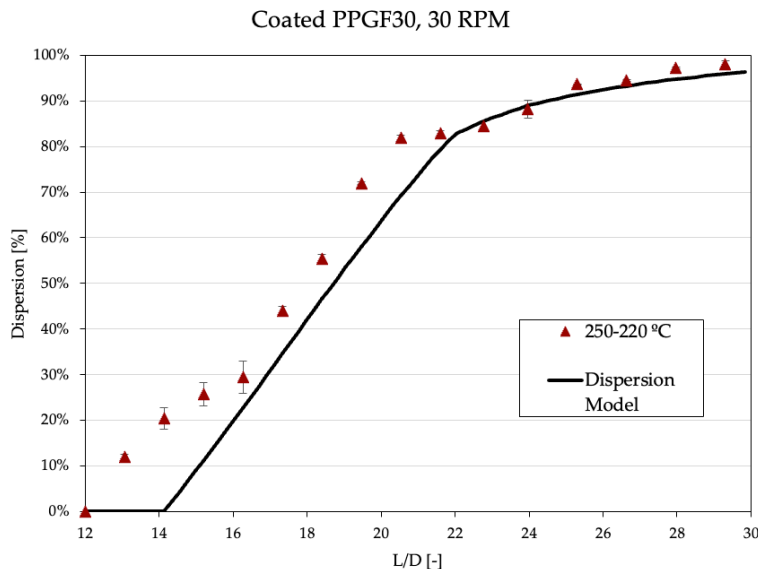


Figure 4.19: Comparison between Experimental data and model for (30 RPM, 250-220°C], PPGF30)

As shown by the results above, the dispersion model has a good fit when compared to experimental results from the screw pull-out experiments. The error difference between the model and experimental values was calculated and can be seen in Figure 4.20. From the figure it can be seen that the majority of the error occurs between the L/D of 13 and 21. This can be attributed back to Figure 4.10, where the curvature assumption is not satisfied by the screw's geometry. In order to more accurately predict deformation in this zone, a deep channel model should be implemented, and curvature should also be taken into account. Table 3 shows the average error difference percentage for each experiment.

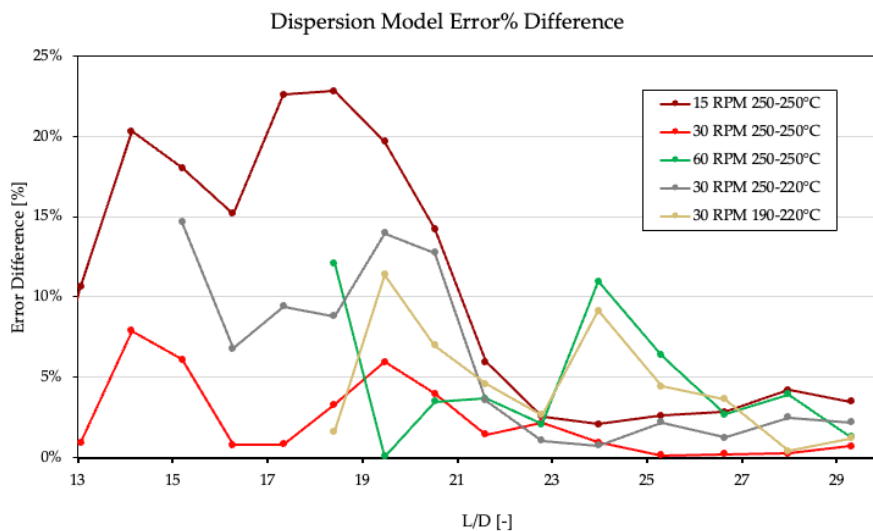


Figure 4.20: Error difference between experimental values and modeled dispersion.

Table 3: Average error difference percentage

Experiment	Error%
15 RPM, 250-250°C	11.1%
30 RPM, 250-250°C	2.3%
60 RPM, 250-250°C	4.9%
30 RPM, 250-220°C	7.4%
30 RPM, 190-220°C	3.6%

A 2D model was also done by implementing the following ordinary differential equation shown in Equation 10. This equation was derived by simply taking the derivative of the dispersion model with respect to z . COMSOL Multiphysics was used to solve a 2-dimensional flow, with geometry similar to Figure 48, where the flow was solved using steady state, isothermal, non-Newtonian properties. The barrel and material temperature were maintained at a constant 250 °C. Results are shown in Figure 4.21, where all the parameters remained the same from the 1D Newtonian model. As shown in the figure, the 2D model under predicts dispersion using the same fitting parameters. Figure 4.22 shows the model with adjusted fitting parameters where k was changed to $11.5e-5$ from $9e-5$. Figure 4.22 also shows how a two-dimensional model distinguishes

dispersion values based on y-axis position where moving wall, which is the barrel in this case, showed larger values of dispersion.

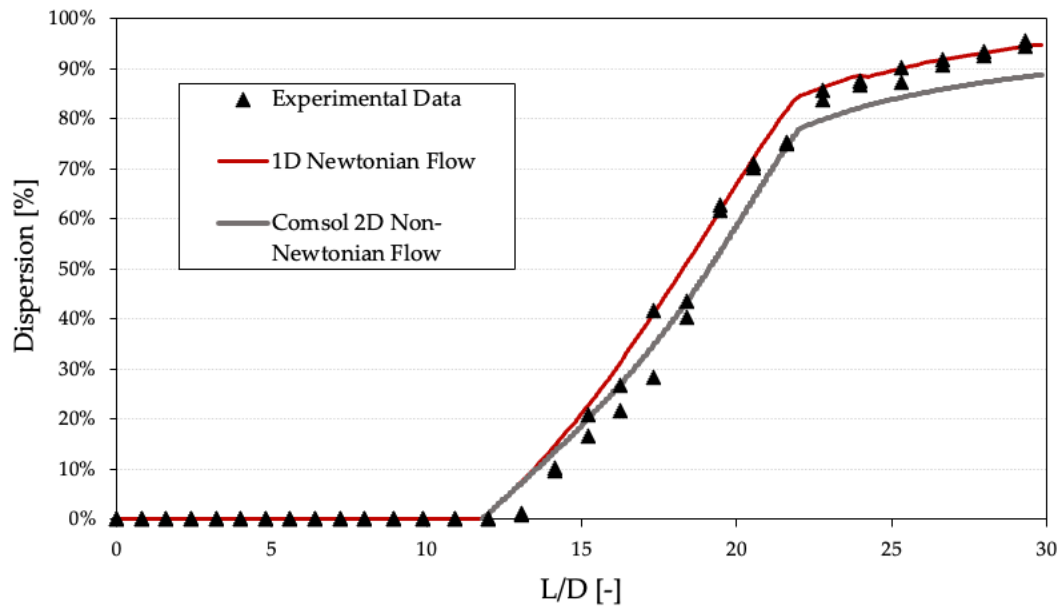


Figure 4.21: Comparison between 1D Newtonian model and 2D COMSOL model using the same fitting parameter (k)

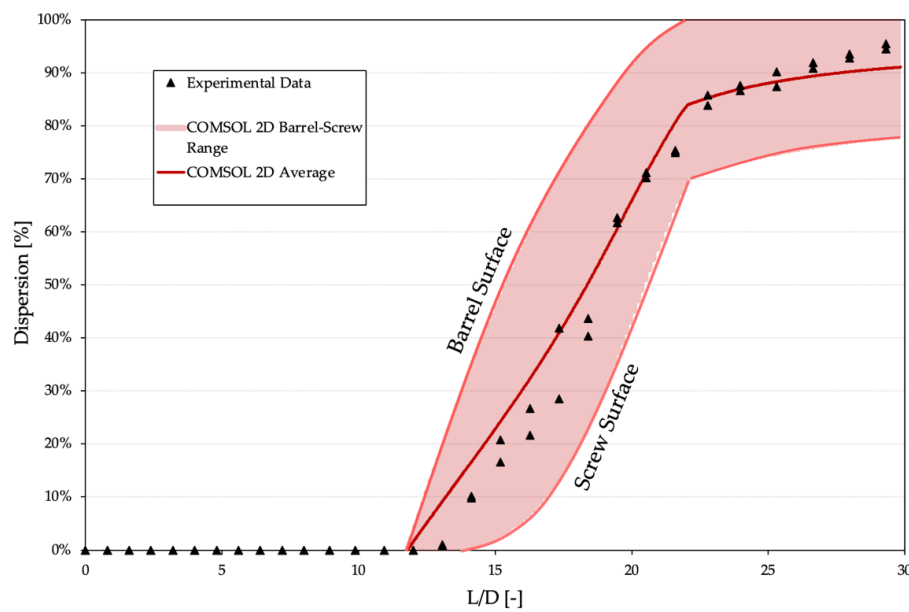


Figure 4.22: Results from the 2D COMSOL model with a different fitting parameter (k) from the 1D model.

4.5 Fiber Length Measurements

As dispersion has successfully been characterized and modeled, fiber length measurements were also done to determine its effect on fiber breakage. For this fiber length study, two samples were taken from every other pitch of the experiment. The fiber length measurement technique developed by the Polymer Engineering Center was used for this study [14,63,69,70]. Two studies were done on this topic; the first study was on different heating profiles for the extruder, while the second study was on comparing coated pellets with pultruded pellets.

Figure 4.23 shows the results of the first study, where the weighted average fiber length is plotted with respect to the modeled dispersion. Past research on this topic has found that most fiber breakage occurs as the material melts or when dispersion is low [23,63]. However, results from this study indicate that both dispersion and fiber breakage begin to occur simultaneously. Most of the samples acquired before dispersion began had all the pellets intact and were being held by a thin melted film. Fiber length measurements of samples with a dispersion of 0% were found to have too much variability and, therefore, were omitted from these figures.

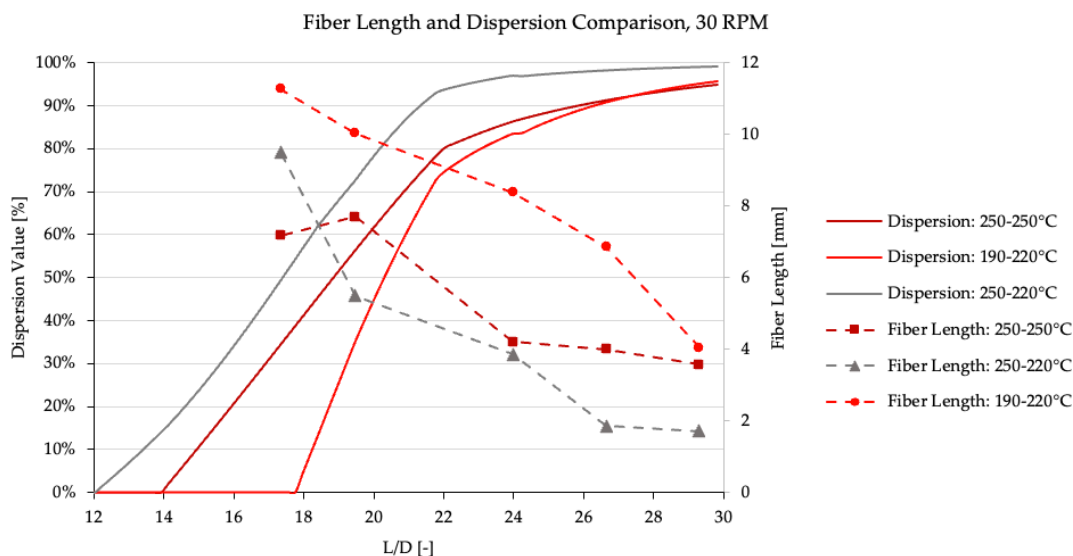


Figure 4.23: Weighted average fiber length compared to modeled fiber dispersion.

Figure 4.24 shows results from the second fiber length study, where coated and pultruded pellets were measured for fiber length and dispersion. It is important to note for this study that pultruded pellets had an initial fiber length of 10 mm and coated pellets had an initial fiber length of 15 mm. The results show that even though pultruded pellets had an initial dispersion much higher than coated pellets, fiber length decreased rapidly and plateaued by an L/D of 21. This gives great insight into the importance of understanding dispersion, as a material could be overprocessed due to fear of low dispersion. This can be seen in Figure 4.24 as the high levels of dispersion only damaged fibers in pultruded pellets for a longer period. In contrast, coated pellets reached a similar level of dispersion and only reached the same level of fiber length as pultruded pellets by the last pitch. Since fiber length and dispersion measurements are time-consuming and difficult, a combination of both dispersion and breakage models can be of great value.

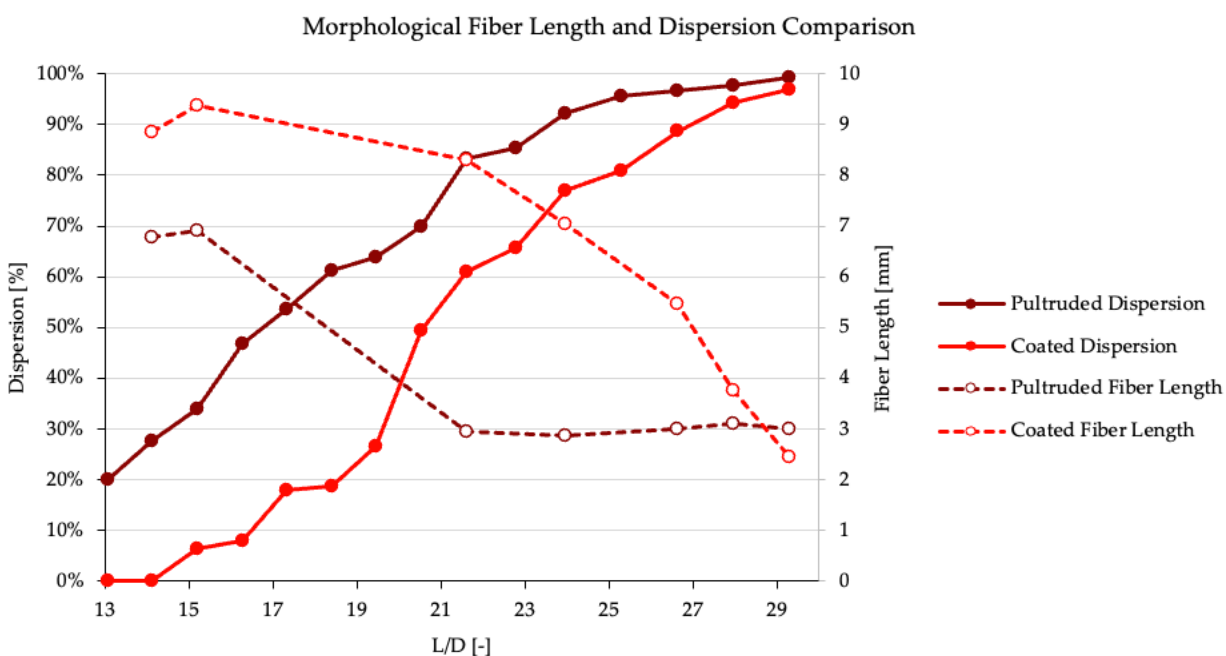


Figure 4.24: Weighted average fiber length compared to measured fiber dispersion.

An initial attempt at modeling fiber length and dispersion was made. The same dispersion model used in the previous section was used in combination with the developed fiber breakage model by Bechara et al[14,63]. Equation 24 shows the

Bechara/Osswald fiber breakage model that was used for this study, where L_W is the weight-average fiber length, $L_{W,\infty}$ is the weighted equilibrium fiber length, and $k_{f,W}$ is a fitting parameter for the fiber breakage model. The same Comsol model from Figure 4.25 was used to calculate both fiber dispersion and breakage. Figure 4.25 shows the results from the Comsol simulation. Results show a correct fiber length trend throughout the screw; However, more fiber length measurements are needed to fully develop a fiber breakage and dispersion model.

$$\frac{dL_W}{dt} + (u \cdot \nabla)L_W = -k_{f,W}(L_W - L_{W,\infty}) \quad (24)$$

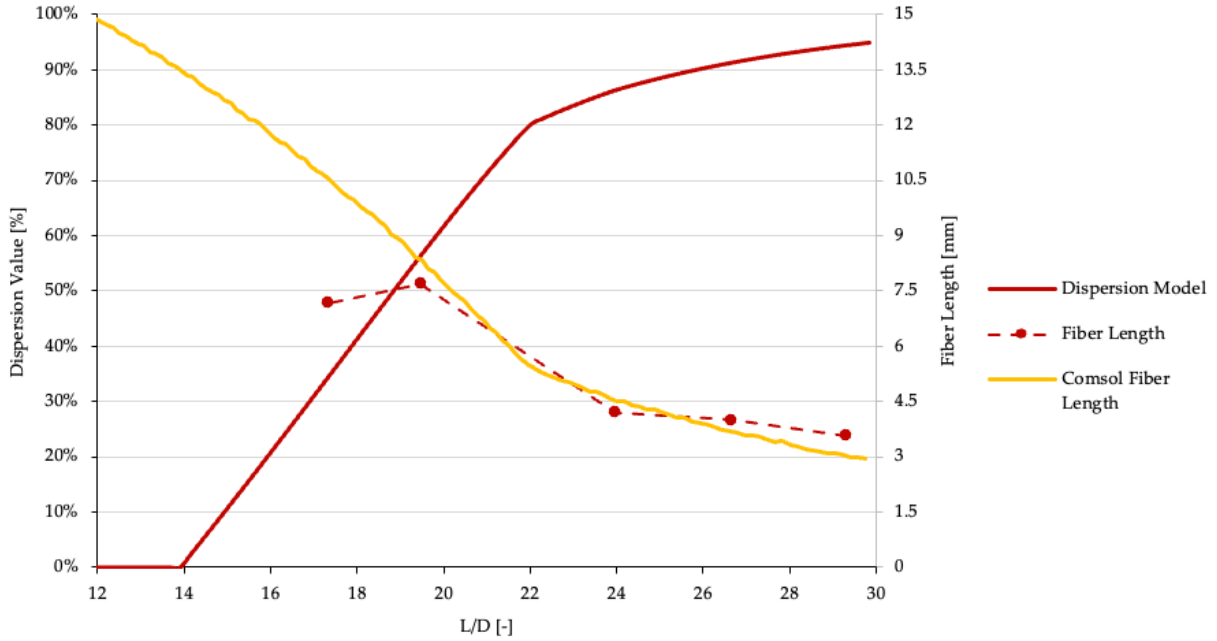


Figure 4.25: Fiber dispersion and fiber breakage model done in Comsol with fiber length measurements.

5. Summary

This dissertation presented a fundamental analysis of fiber dispersion in LFT processing, with the main goal of developing a modeling technique for a single screw extruder. The work focused on five tasks:

- i. To understand the morphological parameters of an LFT pellet that affect dispersion.
- ii. To understand the main driver of fiber dispersion during the plasticizing process.
- iii. To characterize fiber dispersion using an analytical approach.
- iv. To study the dispersion process inside an extruder.
- v. To understand and model fiber dispersion.

Chapter 3 focused on the experimental studies to isolate individual parameters. The single pellet dispersion study aimed at understanding the effect of the pellet fabrication technique on dispersion. A shape parameter was proposed to characterize this effect. The shape parameter had little correlation with dispersion measurements but led to the conclusion that a pellet with smaller fiber content leads to a higher level of dispersion. The multi-pellet dispersion study aimed at isolating the individual parameters that often take effect in a plasticizing unit. A new method to characterize dispersion was developed and led to the development of a dispersion model that was validated with experimental work.

Chapter 4 focused on studying dispersion in the single screw extruder and modeling the phenomena. Screw pull-out experiments were found to be a successful method to determine dispersion within the extruder. A dispersion model that coupled Tadmor's melting model with the equations of motion was developed. The dispersion model was then validated using the screw pull-out data. Fiber length measurements were done on samples used for dispersion study to understand coupled effects.

5.1 Recommendation for Future Work

The dispersion model proposed in this dissertation is the first dispersion model developed. Therefore, there are many other instances where this model can be improved and tested. The first improvement that could be made to the model is to use a more precise method of calculating total deformation within the screw. To do this, it would be necessary to model pressure build-up and validate it with pressure transducers attached to the barrel of the extruder. This calculation of pressure would give a precise measurement of residence time that, coupled with the shear rate, could give a more precise dispersion calculation.

Further morphological studies can distinguish different amounts of fiber content in the pellet. In the single pellet study, it was found that the smaller the fiber content, the faster the fibers dispersed. This understanding of fiber content and dispersion rate can be beneficial to a material fabrication company, as materials can be designed for short extruders or long extruders.

A coupled model of fiber dispersion and breakage would be very beneficial in maintaining fiber length while fully dispersing the fibers. Current fiber breakage models could be explored and tested using fiber length measurements from screw pull-out experiments. A more complex study of the melting phenomena might have to be done in order to determine the exact parameters that affect fiber degradation. Figure 60 shows pellets that were found at the bottom of the hopper during screw pull-out experiments. Pellets seem to be breaking even before any melting actually occurs, making the problem more complex.



Figure 5.1: Broken pellets found at the bottom of the hopper during the screw pull-out experiment.

5.2 Publications

The following articles have been submitted for publication, or are currently work in-progress, as a result of research on modeling fiber attrition:

Perez, H.S., Hohoff, P., Hiller, F., & Osswald, T. (*Forthcoming 2024*) Modeling Fiber Dispersion in a Single Screw Extruder for Long Fiber-Reinforced Thermoplastics.

Perez, H.S., Roman, A.J., Bechara Senior, A., & Osswald, T. (2023). Effect of Fiber Bundle Morphology on Fiber Dispersion for Long Fiber-Reinforced Thermoplastics. *Polymers* 2023, 15(13), 2790; <https://doi.org/10.3390/polym15132790>

Kugler, S. K., Bechara, A., **Perez, H.**, Cruz, C., Kech, A., & Osswald, T. A. (2021). Data enriched lubrication force modeling for a mechanistic fiber simulation of short fiber-reinforced thermoplastics. *Physics of Fluids*, 33(5). <https://doi.org/10.1063/5.0049641>

6. References

- [1] Czerwinski, F., 2021, "Current Trends in Automotive Lightweighting Strategies and Materials," *Materials*, **14**(21).
- [2] Pervaiz, M., Panthapulakkal, S., KC, B., Sain, M., and Tjong, J., 2016, "Emerging Trends in Automotive Lightweighting through Novel Composite Materials," *Materials Sciences and Applications*, **07**(01), pp. 26–38.
- [3] Zhou, W., Cleaver, C. J., Dunant, C. F., Allwood, J. M., and Lin, J., 2023, "Cost, Range Anxiety and Future Electricity Supply: A Review of How Today's Technology Trends May Influence the Future Uptake of BEVs," *Renewable and Sustainable Energy Reviews*, **173**.
- [4] Cheah, L. W., and Heywood, J. B., 2001, *Cars on a Diet: The Material and Energy Impacts of Passenger Vehicle Weight Reduction in the U.S.* Associate Professor of M.
- [5] Mohanty, A. K., Vivekanandhan, S., Tripathi, N., Roy, P., Snowdon, M. R., Drzal, L. T., and Misra, M., 2023, "Sustainable Composites for Lightweight and Flame Retardant Parts for Electric Vehicles to Boost Climate Benefits: A Perspective," *Composites Part C: Open Access*, **12**.
- [6] Shi, X. H., Li, X. L., Li, Y. M., Li, Z., and Wang, D. Y., 2022, "Flame-Retardant Strategy and Mechanism of Fiber Reinforced Polymeric Composite: A Review," *Compos B Eng*, **233**.
- [7] Scaffaro, R., Di Bartolo, A., and Dintcheva, N. T., 2021, "Matrix and Filler Recycling of Carbon and Glass Fiber-reinforced Polymer Composites: A Review," *Polymers (Basel)*, **13**(21).
- [8] Herakovich, Carl. T., 1998, *Mechanics of Fibrous Composites*, John Wiley & Sons, Inc., New York, NY.
- [9] Henning, F., and Heinrich, E., 2005, "LFTs for Automotive Applications," *Reinforced Plastics*, **49**(2), pp. 24–33.

- [10] Bigg, D. M., 1985, "Effect of Compounding on the Properties of Short Fiber Reinforced Injection Moldable Thermoplastic Composites," *Polym Compos*, **6**(1).
- [11] Gandhi, U. N., Goris, S., Osswald, T. A., and Song, Y.-Y., *Discontinuous Fiber-Reinforced Composites Fundamentals and Applications*.
- [12] Truckenmuller, F., and Fritz, H.-G., 1991, "Injection Molding of Long Fiber-Reinforced Thermoplastics: A Comparison of Extruded and Pultruded Materials With Direct Addition of Roving Strands," *Polym Eng Sci*, **31**(18).
- [13] Thomason, J. L., Owens, E., and Fiberglas, C., 2002, "The Influence of Fibre Length and Concentration on the Properties of Glass Fibre Reinforced Polypropylene: 5. Injection Moulded Long and Short Fibre PP," *Composites: Part A*, **33**, pp. 1641–1652.
- [14] Bechara, A., 2021, "Modeling Fiber Damage During Processing of Long Fiber-Reinforced Thermoplastic Composites," University of Wisconsin-Madison.
- [15] Gupta, V. B., Mittal, R. K., Sharma, P. K., Mennig, G., and Wolters, J., 1989, "Some Studies on Glass Fiber-reinforced Polypropylene. Part I: Reduction in Fiber Length during Processing," *Polym Compos*, **10**(1), pp. 8–15.
- [16] Gupta, V. B., Mittal, R. K., Sharma, P. K., Mennig, G., and Wolters, J., 1989, "Some Studies on Glass Fiber-reinforced Polypropylene. Part II: Mechanical Properties and Their Dependence on Fiber Length, Interfacial Adhesion, and Fiber Dispersion," *Polym Compos*, **10**(1), pp. 16–27.
- [17] Cattanach, J. B., Guff, G., and Cogswell, F. N., 1986, "The Processing of Thermoplastics Containing High Loadings of Long and Continuous Reinforcing Fibers," *Polymer Engineering*, **6**(1).
- [18] Kelleher, P. G., 1990, "Report on the State of the Art: Injection Molding of Fiber Reinforced Thermoplastics. Part I. Materials and Processes," *Advances in Polymer Technology*, **10**(3), pp. 219–230.

- [19] von Turkovich, R., and Erwin, L., 1983, "Fiber Fracture in Reinforced Thermoplastic Processing," *Polym Eng Sci*, **23**(13), pp. 743–749.
- [20] Inoue, A., Morita, K., Tanaka, T., Arao, Y., and Sawada, Y., 2015, "Effect of Screw Design on Fiber Breakage and Dispersion in Injection-Molded Long Glass-Fiber-Reinforced Polypropylene," *J Compos Mater*, **49**(1), pp. 75–84.
- [21] Larock, J. A., Hahn, H. T., Evans, D. J., and Bank, A., 1989, "Pultrusion Processes for Thermoplastic Composites Pleasantville Industrial Park," *Journal of Thermoplastic Composite Materials*, **2**(3), pp. 216–229.
- [22] Bijsterbosch, H., and Gaymans, R. J., 1995, "Polyamide 6-Long Glass Fiber Injection Moldings," *Polym Compos*, **16**(5), pp. 363–369.
- [23] Wolf, H. J., 1994, "Screw Plasticating of Discontinuous Fiber Filled Thermoplastic: Mechanisms and Prevention of Fiber Attrition," *Polym Compos*, **15**(5), pp. 375–383.
- [24] Zhang, D., He, M., Qin, S., and Yu, J., 2017, "Effect of Fiber Length and Dispersion on Properties of Long Glass Fiber Reinforced Thermoplastic Composites Based on Poly(Butylene Terephthalate)," *RSC Adv*, **7**(25), pp. 15439–15454.
- [25] Osswald, T. A., 2010, *Understanding Polymer Processing*, Hanser, Munich, Germany.
- [26] Osswald, T., and Menges, G., 2012, *Material Science of Polymers for Engineers*, Hanser, Munich.
- [27] Osswald, T. A., and Randall, C., 2011, *Understanding Polymer Processing 1st ed*, Hanser, Munich.
- [28] Baur, E., Drummer, D., Osswald, T.A., Rudolph, N., 2022, *Saechtling Kunststoff-Handbuch: Eigenschaften*, Hanser, Munich.
- [29] Marschik, C., Roland, W., and Osswald, T. A., 2022, "Melt Conveying in Single-Screw Extruders: Modeling and Simulation," *Polymers (Basel)*, **14**(5).
- [30] Wilczyński, K., Nastaj, A., Lewandowski, A., Krzysztof Wilczyński, K., and Buziak, K., 2019, "Fundamentals of Global Modeling for Polymer Extrusion," *Polymers (Basel)*, **11**(12).

- [31] Tadmor, Z., and Gogos, C. G., 2006, *Tadmor-Gogos*, John Wiley & Sons, Hoboken, New Jersey.
- [32] Tadmor, Z., and Imrich Klein, 1970, *Engineering Principles of Plasticating Extrusion*, Van Nostrand Reinhold Company, New York.
- [33] Broyer, E., and Tadmor, Z., 1972, "Solids Conveying in Screw Extruders Part I: A Modified Isothermal Model," *Polym Eng Sci*, **12**(1), pp. 12–24.
- [34] Wilczyński, K., Buziak, K., Wilczyński, K. J., Lewandowski, A., and Nastaj, A., 2018, "Computer Modeling for Single-Screw Extrusion of Wood-Plastic Composites," *Polymers (Basel)*, **10**(3).
- [35] Darnell, W. H., and Mol, E. A. J., 1956, "Solids Conveying in Extruders," *SPE J*, **20**, pp. 20–29.
- [36] Schneider, K., 1968, "Der Fördervorgang in Der Einzugszone Eines Extruders," Rheinisch-Westfälische Technische Hochschule Aachen.
- [37] Hyun, K. S., Spalding, M. A., and Hinton, C. E., 1997, "Theoretical and Experimental Analysis of Solids Conveying in Single-Screw Extruders," *Journal of Reinforced Plastics and Composites*, **16**, pp. 1210–1219.
- [38] Tadmor, Z., and Klein, I., 1970, *Engineering Principles of Plasticating Extrusion*, van Nostrand Reinhold, New York [u.a.
- [39] Kacir, L., and Tadmor, Z., 1972, "Solids Conveying in Screw Extruders Part III: The Delay Zone," *Polym Eng Sci*, **12**(5), pp. 387–395.
- [40] Tadmor, Z., and Broyer, E., 1972, "Solids Conveying in Screw Extruders Part II: Non-Isothermal Model," *Polym Eng Sci*, **12**(5), pp. 378–386.
- [41] Maddock, B. H., 1959, "A Visual Analysis of Flow and Mixing in Extruder Screws," *SPE ANTEC Tech. Papers*, **15**(383).
- [42] Street, L. F., 1961, "Plastifying Extrusion," *International Plastics Engineering*, **1**, pp. 289–296.

- [43] Zhu, F., 2001, *Extrusion Theory and Application*, China Light Industry Press, Beijing, China.
- [44] Del Pilar Noriega, M., Osswald, T. A., and Ferrier, N., 2004, "In Line Measurement of the Polymer Melting Behavior in Single Screw Extruders," *Journal of polymer engineering*.
- [45] Klein, I., and Marshall, D., 1968, *Computer Programs for Plastic Engineers*, Reinhold Book Corporation.
- [46] Syrjala, S., 2000, "A New Approach for the Simulation of Melting in Extruders," *International Communications Heat Mass*, **27**, pp. 623–634.
- [47] Viriyayuthakorn, M., and Kassahun, B., 1985, "A Three Dimensional Model for Plasticating Extrusion Screw Design," *SPE-ANTEC Technical Papers*, **30**, pp. 81–84.
- [48] Rauwendaal, C., Osswald, T. A., Tellez, G., and Gramann, P. J., 1998, *Flow Analysis in Screw Extruders-Effect of Kinematic Conditions*.
- [49] Rauwendaal, C., 2014, *Polymer Extrusion*, Hanser, Munich.
- [50] Bird, R. B., Stewart, W. E., Lightfoot, E. N., and Klingenberg, D. J., 2015, *Introductory Transport Phenomena*, John Wiley & Sons.
- [51] Osswald, T., and Hernandez-Ortiz, J., 2006, *Polymer Processing: Modeling and Simulation*, Hanser, Munich.
- [52] Manas-Zloczower, I., 2009, *Mixing and Compounding of Polymers*.
- [53] Powell, R. L., and Mason, S. G., 1982, "Dispersion by Laminar Flow," *AIChE Journal*, **28**(2), pp. 286–293.
- [54] Rwei, S. P., and Manas-Zloczower, I., 1991, "Characterization of Agglomerate Dispersion by Erosion in Simple Shear Flows," *Polym Eng Sci*, **31**(8), pp. 558–562.
- [55] Boyle, J. F., Manas-Zloczower, I., and Feke, D. L., 2005, "Hydrodynamic Analysis of the Mechanisms of Agglomerate Dispersion," *Powder Technol*, **153**(2), pp. 127–133.

- [56] Scurati, A., Feke, D. L., and Manas-Zloczower, I., 2005, "Analysis of the Kinetics of Agglomerate Erosion in Simple Shear Flows," *Chem Eng Sci*, **60**(23), pp. 6564–6573.
- [57] Rwei, S. P., and Manas-Zloczower, I., 1990, "Observation of Carbon Black Agglomerate Dispersion in Simple Shear Flows," **30**(12), pp. 701–706.
- [58] Manas-Zloczower, I., and Feke, D. L., 1989, "Analysis of Agglomerate Rupture in Linear Flow Fields," *International Polymer Processing*, **4**(1), pp. 3–8.
- [59] Gopalkrishnan, P., Manas-Zloczower, I., and Feke, D. L., 2007, "Effect of Morphology and Extent of Infiltration on the Cohesivity and Dispersion Mechanisms of Particle Agglomerates," *Chem Eng Sci*, **62**(14), pp. 3740–3747.
- [60] Domingues, N., Camesasca, M., Kaufman, M., Manas-Zloczower, I., Gaspar-Cunha, A., and Covas, J. A., 2010, "Modeling of Agglomerate Dispersion in Single Screw Extruders," *International Polymer Processing*, **25**(3), pp. 251–257.
- [61] Horwatt, S. W., Manas-Zloczower, I., and Feke, D. L., *DISPERSION BEHAVIOR OF HETEROGENEOUS AGGLOMERATES AT SUPERCRITICAL STRESSES*.
- [62] Manas-Zloczower, I., 185AD, "Analysis of Agglomerate Separation in Linear Flow Field," *International Polymer Processing*, **2**(3–4), pp. 185–190.
- [63] Bechara, A., Goris, S., Yanev, A., Brands, D., and Osswald, T., 2021, "Novel Modeling Approach for Fiber Breakage during Molding of Long Fiber-Reinforced Thermoplastics," *Physics of Fluids*, **33**(7), p. 1ENG.
- [64] Ren, P., and Dai, G., 2014, "Fiber Dispersion and Breakage in Deep Screw Channel during Processing of Long Fiber-Reinforced Polypropylene," *Fibers and Polymers*, **15**(7), pp. 1507–1516.
- [65] Kuroda, M. M. H., and Scott, C. E., 2002, "Initial Dispersion Mechanisms of Chopped Glass Fibers in Polystyrene," *Polym Compos*, **23**(3), pp. 395–405.
- [66] Simon, S. A., Bechara Senior, A., and Osswald, T., 2020, "Experimental Validation of a Direct Fiber Model for Orientation Prediction," *Journal of Composites Science*, **4**(2), p. 59.

- [67] Giacomini, A. J., Samurkas, T., and Dealy, J. M., 1989, "A Novel Sliding Plate Rheometer for Molten Plastics," *Polymer Engineering & Science*, **29**(8), pp. 499-504.
- [68] Manikandan, S., 2011, "Measures of Dispersion," *J Pharmacol Pharmacother*, **2**(4), pp. 315-316.
- [69] Goris, S., Simon, S., Montoya, C., Bechara, A., Candal, M. V., Brands, D., Yanev, A., and Osswald, T. A., 2017, "Experimental Study on Fiber Attrition of Long Glass Fiber-Reinforced Thermoplastics under Controlled Conditions in a Couette Flow," Annual technical conference and exhibition-Society of Plastics Engineers.
- [70] Goris, S., Back, T., Yanev, A., Brands, D., Drummer, D., and Osswald, T. A., 2018, "A Novel Fiber Length Measurement Technique for Discontinuous Fiber-Reinforced Composites: A Comparative Study with Existing Methods," *Polym Compos*, **39**(11), pp. 4058-4070.